COMPUTATIONAL INVESTIGATION OF TRANSPORT PHENOMENA IN ADSORPTION BED

A THESIS SUBMITTED TO
THE GRADUATE SCHOOL OF NATURAL AND APPLIED SCIENCES
OF
MIDDLE EAST TECHNICAL UNIVERSITY

BY

SILAY ÖNDER

IN PARTIAL FULFILLMENT OF THE REQUIREMENTS
FOR
THE DEGREE OF MASTER OF SCIENCE
IN
CHEMICAL ENGINEERING

SEPTEMBER 2023

Approval of the thesis:

COMPUTATIONAL INVESTIGATION OF TRANSPORT PHENOMENA IN ADSORPTION BED

submitted by **SILAY ÖNDER** in partial fulfillment of the requirements for the degree of **Master of Science in Chemical Engineering Department, Middle East Technical University** by,

Prof. Dr. Halil Kalıpçılar
Dean, Graduate School of **Natural and Applied Sciences** _____

Prof. Dr. Pınar Çalık
Head of Department, **Chemical Engineering** _____

Prof. Dr. Yusuf Uludağ
Supervisor, **Chemical Engineering, METU** _____

Prof. Dr. Gürkan Karakaş
Co-supervisor, **Chemical Engineering, METU** _____

Examining Committee Members:

Prof. Dr. Levent Yılmaz
Chemical Engineering, METU _____

Prof. Dr. Yusuf Uludağ
Chemical Engineering, METU _____

Prof. Dr. Gürkan Karakaş
Chemical Engineering, METU _____

Prof. Dr. Kerim Yapıcı
Chemical Engineering, Suleyman Demirel University _____

Assoc. Prof. Dr. Harun Koku
Chemical Engineering, METU _____

Date:08.09.2023

I hereby declare that all information in this document has been obtained and presented in accordance with academic rules and ethical conduct. I also declare that, as required by these rules and conduct, I have fully cited and referenced all material and results that are not original to this work.

Name, Surname: Sılay Önder

Signature :

ABSTRACT

COMPUTATIONAL INVESTIGATION OF TRANSPORT PHENOMENA IN ADSORPTION BED

Önder, Sılay
M.S., Department of Chemical Engineering
Supervisor: Prof. Dr. Yusuf Uludağ
Co-Supervisor: Prof. Dr. Gürkan Karakaş

September 2023, 86 pages

The world's rising level of energy usage with increasing population has become a high-priority issue with the depletion of energy sources. Nowadays, researchers concentrate on developing environmentally friendly energy technologies and utilizing available waste heat sources. Chemical heat pump systems are a promising way of sustainable waste heat recovery because of their large storage capacity, long-term reactant and product storage, and reduced heat loss. Adsorption-based chemical heat pumps have further useful advantages in this category. Yet, there are still many practical issues that are ongoing research areas. One of the main disadvantages is the poor heat and mass transfer characteristic of the packed bed systems and the low thermal conductivity of the adsorbent. Therefore, improving the poor heat and mass transfer characteristics of the packed adsorption bed in the design step is crucial. Several modelling approaches are available in the literature for packed bed systems. However, conventional pseudo-homogeneous and heterogeneous models are insufficient to capture all the complex phenomena happening due to local porosity distribution.

In this study, a theoretical and computational model to simulate the ethanol/acti-

vated carbon pairing adsorption bed was developed using particle-resolved Computational Fluid Dynamics approach. First, the reactor bed was 3D-modelled and then simulated. Random packing structure of the bed was generated by Discrete Element Method using commercial Altair EDEM software and the cylindrical reactor was packed with spherical particles. Then the mesh generation for 3D geometry packed with spherical particles was performed using commercial preprocessor ANSYS ICEM CFD software. Contact point treatment studies were conducted to avoid skewness and achieve good-quality mesh for CFD simulations. ANSYS Fluent software was used for the CFD simulations of the developed mesh model. Multiscale modelling of the bed was performed based on continuity, momentum, energy equations and adsorption model. This study thoroughly explains the transport properties of both the intra-particle and the interstitial fluid region in a randomly packed adsorption bed with small tube-to-particle diameter ratio. The procedure can be utilized for the design of catalyst particles and reactors for randomly packed adsorption beds.

Keywords: modelling, CFD, adsorption, packed bed

ÖZ

ADSORPSİYON YATAĞINDAKİ TAŞINIM OLAYLARININ HESAPLAMALI İNCELENMESİ

Önder, Sılay
Yüksek Lisans, Kimya Mühendisliği Bölümü
Tez Yöneticisi: Prof. Dr. Yusuf Uludağ
Ortak Tez Yöneticisi: Prof. Dr. Gürkan Karakaş

Eylül 2023 , 86 sayfa

Dünyada artan nüfusla birlikte artan enerji kullanımı, enerji kaynaklarının tükenmesiyle birlikte öncelikli bir konu haline gelmiştir. Günümüzde araştırmacılar çevre dostu enerji teknolojileri geliştirmeye ve mevcut atık ısı kaynaklarından yararlanmaya odaklanmaktadır. Kimyasal ısı pompası sistemleri, geniş depolama kapasiteleri, uzun vadeli reaktan ve ürün depolamaları ve azaltılmış ısı kaybı nedeniyle sürdürülebilir atık ısı geri kazanımının umut verici bir yoludur. Adsorpsiyon bazlı kimyasal ısı pompalarının bu kategoride başka yararlı avantajları da vardır. Ancak halen devam eden araştırma alanları olan pek çok pratik sorun bulunmaktadır. Ana dezavantajlardan biri, dolgulu yatak sistemlerinin zayıf ısı ve kütle transfer özelliği ve adsorbanın düşük ısıl iletkenliğidir. Bu nedenle tasarım aşamasında dolgulu adsorpsiyon yatağının zayıf ısı ve kütle transfer özelliklerinin iyileştirilmesi çok önemlidir. Dolgulu yatak sistemleri için literatürde çeşitli modelleme yaklaşımları mevcuttur. Ancak geleneksel sözde homojen ve heterojen modeller, yerel gözeneklilik dağılımı nedeniyle meydana gelen tüm karmaşık olayları yakalamak için yeterli değildir.

Bu çalışmada, parçacık çözümlü Hesaplamalı Akışkanlar Dinamiği yaklaşımı kullanılarak etanol/aktif karbon adsorpsiyon yatağını simüle etmek için teorik ve hesaplamalı bir model geliştirildi. Öncelikle reaktör yatağı 3 boyutlu olarak modellendi ve ardından simüle edildi. Yatağın rastgele doldurulmuş yapısı, ticari EDEM yazılımı kullanılarak Ayrık Elemanlar Yöntemi ile oluşturuldu ve silindirik reaktör, küresel parçacıklarla dolduruldu. Daha sonra küresel parçacıklarla dolu 3 boyutlu geometri için ağ oluşturma işlemi ticari ön işlemci ICEM CFD yazılımı kullanılarak gerçekleştirildi. Çarpıklığı önlemek ve CFD simülasyonları için iyi kalitede ağ elde etmek amacıyla temas noktası iyileştirme çalışmaları yürütüldü. Geliştirilen ağ modelinin CFD simülasyonları için ANSYS Fluent yazılımı kullanıldı. Yatağın çok ölçekli modellemesi süreklilik, momentum, enerji denklemleri ve adsorpsiyon modeline dayalı olarak yapıldı. Bu çalışma, küçük tüp-partikül çapı oranına sahip rastgele doldurulmuş adsorpsiyon yatağında hem partikül içi hem de interstisyel akışkan bölgesinin taşıma özelliklerinin kapsamlı bir şekilde anlaşılmasını sağlar. Prosedür, rastgele doldurulmuş adsorpsiyon yatakları için katalizör parçacığının ve reaktörün tasarımında kullanılabilir.

Anahtar Kelimeler: modelleme, CFD, adsorpsiyon, dolgulu yatak

To my family

ACKNOWLEDGMENTS

I would like to express my deepest appreciation to my supervisors Prof. Dr. Yusuf Uludağ and Prof. Dr. Gürkan Karakaş for their guidance, mentorship and aid that helped me to improve both myself and my research. These outcomes would not have been obtained without their support, patience and valuable recommendations.

I would like to extend my sincere thanks to Nurkan Sarohan for providing the help I needed any time while working on both this thesis and as an assistant, especially in recent times that are challenging. I would also specially thank İklim Gökçe for her support, friendship and joy that she brought and shared in this journey.

I am also deeply indebted to the suggestions Berkan Atman gave me and any kind of brain-storming that I needed for this thesis. Anything that we discussed was so important for this thesis to have progress and the support was invaluable. I would also to thank Soner Yaşar for the aid and discussions about Fluent and FVM that also helped for the improvements of this work.

I am also grateful for all the help provided by Recep Can Keçeci and Çağatay Önder on 3D modelling and geometry generation. I sincerely appreciate the provision of the computer by Recep Can Keçeci that sped up all my runs. Lastly, I thank Bora Yalçıner with all my sincerety for answering all my silly questions, aiding in my programming mistakes and for emotional support that helped me to proceed anytime.

TABLE OF CONTENTS

LIST OF TABLES

TABLES

LIST OF FIGURES

FIGURES

LIST OF ABBREVIATIONS

2D	2 Dimensional
3D	3 Dimensional
AC	Activated carbon
AHP	Adsorption Heat Pump
CFD	Computational Fluid Dynamics
CHP	Chemical Heat Pump
DEM	Discrete Element Method
DNS	Direct Numerical Simulation
FEM	Finite Element Method
FVM	Finite Volume Method
LES	Large-Eddy Simulations
LBM	Lattice-Boltzmann Method
RANS	Reynolds-Averaged Navier-Stokes Equations

LIST OF SYMBOLS

Latin letters

ΔH_{ads}	heat of adsorption	$\mathrm{J\,mol^{-1}}$
C_p	specific heat capacity	$\mathrm{J\,kg^{-1}\,K^{-1}}$
C_{p,C_2H_5OH}	specific heat capacity of ethanol	$\mathrm{J\,kg^{-1}\,K^{-1}}$
C_{p,N_2}	specific heat capacity of nitrogen	$\mathrm{J\,kg^{-1}\,K^{-1}}$
$C_{p,s}$	specific heat capacity of solid	$\mathrm{J\,kg^{-1}\,K^{-1}}$
d_p	particle diameter	m
$D_{eff,knud}$	effective Knudsen diffusion coefficient	$\mathrm{m^2\,s^{-1}}$
$D_{i,m}$	molecular diffusion coefficient	$\mathrm{m^2\,s^{-1}}$
d_{pore}	pore diameter	nm
E	Young's modulus	$\mathrm{N\,m^{-2}}$
e	coefficient of restiturion	[−]
F_c	contact forces	N
F_g	gravitational force	N
F_n	normal force	N
F_s	forces acting on particle's surface	N
F_t	tangential force	N
G	shear modulus	$\mathrm{N\,m^{-2}}$
h	enthalpy	$\mathrm{J\,kg^{-1}}$
h_f	enthalpy of fluid	$\mathrm{J\,kg^{-1}\,K}$

h_s	enthalpy of solid	$\mathrm{J\,kg^{-1}}$
J_i	diffusion mass flux	$\mathrm{kg\,m^{-2}\,s}$
k	turbulent kinetic energy	J
k_f	thermal conductivity of fluid	$\mathrm{W\,m^{-1}\,K^{-1}}$
m	mass	kg
M_A	molecular weight of species A	$\mathrm{g\,mol^{-1}}$
M_B	molecular weight of species B	$\mathrm{g\,mol^{-1}}$
m_p	mass of particle	kg
MW_i	molecular weight of species$i$	$\mathrm{kg\,mol^{-1}}$
N_t	tangential damping	$\mathrm{N\,s\,m^{-1}}$
p	pressure	Pa
P_s	saturation pressure	bar
R	ideal gas constant	$\mathrm{J\,mol^{-1}\,K^{-1}}$
R	radius	m
Re_p	particle Reynolds number	[–]
S_t	tangential stiffness	$\mathrm{N\,m^{-1}}$
Sc_t	turbulent Schmidt number	[–]
v	velocity	$\mathrm{m\,s^{-1}}$
v_0	inlet velocity	$\mathrm{m\,s^{-1}}$
V_A	diffusion molar volume of species A	[–]
V_B	diffusion molar volume of species B	[–]
W	adsorption capacity	$\mathrm{kg\,C_2H_5OH\,kg^{-1}\,AC}$
w	adsorbed amount	$\mathrm{kg\,C_2H_5OH\,kg^{-1}\,AC}$

Y_i	mass fraction of species i	$[-]$

Greek letters

δ_n	normal overlap	m
δ_n	tangential overlap	m
ϵ	porosity	$[-]$
μ	molecular viscosity	Pa s
μ_r	coefficient of rolling friction	$[-]$
μ_s	coefficient of static friction	$[-]$
μ_t	eddy viscosity	Pa s
ν	Poisson's ratio	$[-]$
ρ	density	$\mathrm{kg\,m^{-3}}$
ρ_f	density of fluid	$\mathrm{kg\,m^{3}}$
ρ_f	density of fluid	$\mathrm{kg\,m^{-3}}$
ρ_s	density of solid	$\mathrm{kg\,m^{-3}}$
τ_{ij}	stress tensor	N

CHAPTER 1

INTRODUCTION

Increasing worldwide energy insufficiency led recent studies to focus on low-grade heat utilization since waste heat generation is inevitable for most process industries; however, there is a shortcoming of waste heat recovery. Using an appropriate heat pump in combination with a low-temperature heat source raises its temperature to a higher level. Despite the fact that vapor compression heat pumps and vapor absorption heat pumps are typical for this purpose, in recent years, chemical heat pump systems have drawn attention due to their suitability for waste heat recovery [6]. Chemical heat pumps can be operated to upgrade low-temperature heat sources to high temperature as well as for energy storage without the necessity of mechanical energy conversion or electrical power as opposed to conventional heat pumps. Therefore, waste heat recovery by chemical heat pumps may be an effective solution in terms of energy efficiency since they are not electrically driven and, in terms of sustainability since they do not require refrigerants that lead to greenhouse gas emissions[7].

A chemical heat pump system consists of one evaporator, one condenser, and one or two reactors, and it typically uses reversible reactions for the storage and release of energy, making the reactor bed a key component in the system. While a reversible chemical reaction may take place in the reactor section, absorption/reabsorption of metal hydrides or adsorption/desorption of adsorbate gases to solid adsorbents may also take place in CHP systems [6]. Among these kinds of chemical heat pumps, adsorption-based heat pumps have drawn the attention of researchers in recent years due to having some practical advantages. Adsorption heat pumps can be additionally categorized as chemisorption heat pumps and physisorption heat pumps. Chemisorption is fueled by a chemical reaction that takes place at the exposed surface. The

adsorbate and adsorbent are chemically bonded (with either ionic or covalent bonds) due to the strong interaction forces between them. On the other hand, physisorption is based on Van der Waals forces with very weak interaction energy [7]. The essential property of adsorption-based heat pumps is to allow for the recurrence of the same cycle; the process of adsorption and desorption must be reversible.

Adsorption heat pump systems that are based on physical adsorption use no corrosive chemical substances. In addition, adsorbent-adsorbate pairs can be used long-term because they do not have salt corrosion problems, and they do not have to be replaced for short intervals compared to the absorbates in absorption systems [8]. Figure 1.1 shows the basic thermodynamic cycle of an adsorption-based chemical heat pump. In the D-A path, the valve between the adsorbent bed and the condenser is closed, and the valve between the evaporator and the adsorbent bed is opened. Isobaric adsorption occurs at this stage and adsorption heat is released. Then, the valve between the evaporator and the bed is closed and the system is started to be heated for the preparation of the desorption stage. When the system reaches the condenser pressure, the valve between the bed and the condenser is opened which continues with the isobaric desorption in the B-C path. The desorbed phase moves from the bed to the condenser where it condenses and releases valuable condensational heat. Similar to the A-B path, heat removal occurs after the valves between the bed and condenser and evaporator are closed in the C-D path for the next adsorption stage.

Some of the typical adsorbent-adsorbate combinations utilized in adsorption heat pump systems are zeolite-water, active carbon-methanol, active carbon-ethanol, silica gel-water, and carbon-ammonia [9]. It is important for adsorbate to have high latent heat, to be suitable for the environment in terms of corrosivity and toxicity, and to have stability in the operating temperature and pressure range. On the other hand, the important properties of adsorbents are high adsorption capacity, high thermal conductivity as well as being stable thermally [8]. Such specifications of the working pairs of the bed should be made in addition to researching the heat of adsorption values, energy density, working temperature ranges and the specific heat of adsorption. The fact that water has a high latent heat of vaporization, is abundant, and poses no risks when used as a refrigerant may make water appear as the best adsorbate; however, its low vapor pressure near 0 °C and 0 °C freezing temperature makes it challenging to

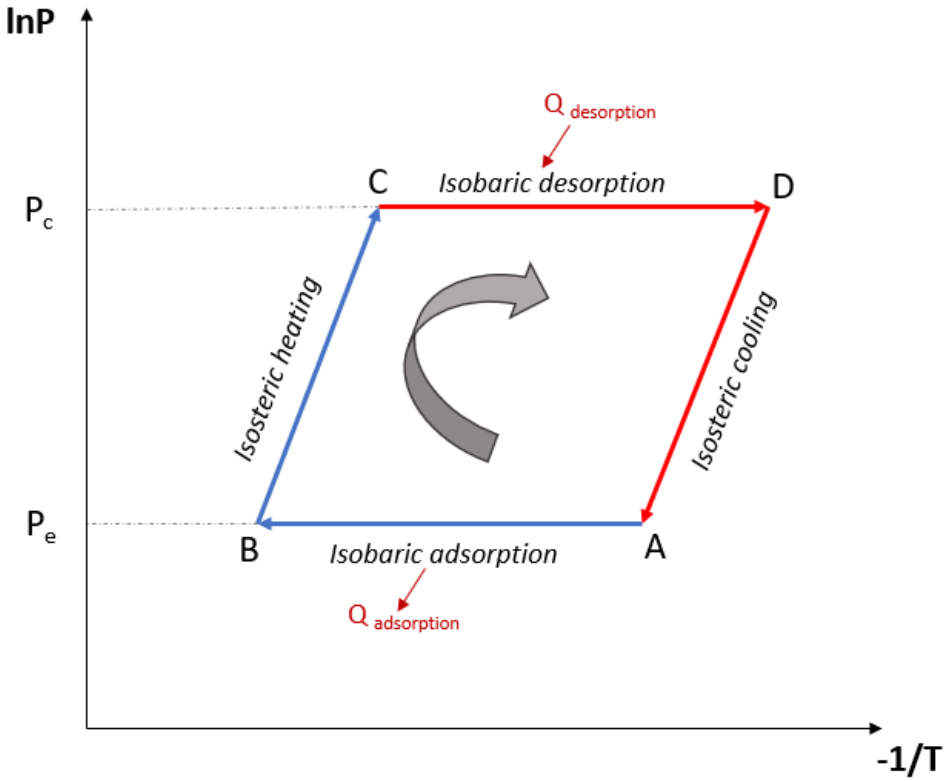

Figure 1.1: Clapeyron diagram of an adsorption heat pump.

be utilized as a refrigerant [9]. Additionally, zeolite-water pair was reported to have low adsorption capacity; thus, activated carbon-ethanol working pair gained attention [10]. Due to having low freezing point, good chemical stability, nontoxicity, no risk of ozone depletion, minimal potential for global warming, and low cost of industrial manufacture, ethanol has been proposed as a possible refrigerant [11]. Attan et al. [12] noted that activated-carbon fiber demonstrated good absorptivity for a variety of refrigerants, including water, ammonia, acetone, methanol, and ethanol. Activated-carbon fiber also has a high specific surface area, large total pore volume, and narrow average pore size.

The objective of this thesis is to focus on the packed adsorption bed design rather than concentrating on the heat pump design. Modelling and simulating the bed allows us to observe the transport characteristics of the complex geometry bed with varying structural parameters and operating conditions which will aid in improving poor heat and mass transfer characteristics of the bed in the design step. Since the

hydrodynamics characteristics affect the performance of the adsorption bed, a more accurate representation of the momentum field was targeted to capture all the transport characteristics. Hence, 3D DEM-CFD simulations of a randomly packed model were utilized in this study. The model can be adapted to an adsorption bed of an AHP with ethanol/activated carbon working pairs and may also be used for different variations of adsorption-packed beds.

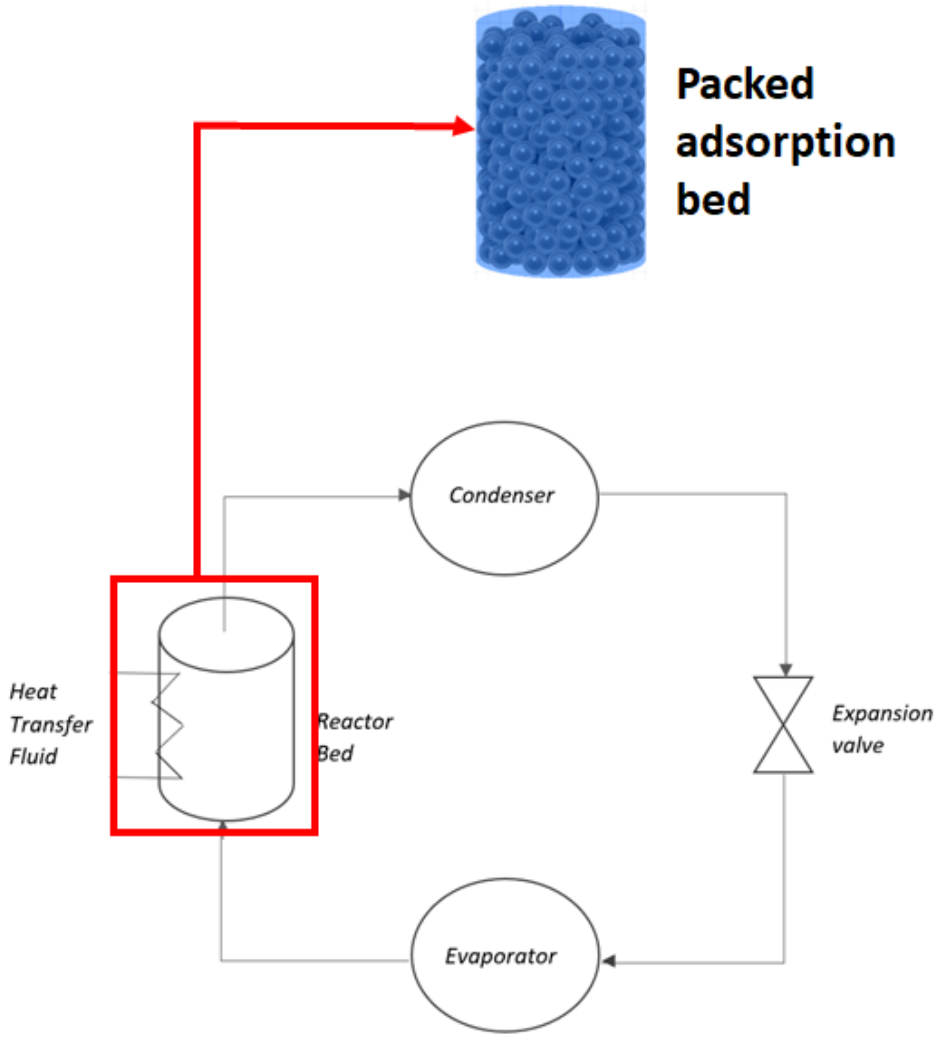

Figure 1.2: A scheme of a single-bed AHP.

CHAPTER 2

LITERATURE REVIEW

Modelling packed bed systems can be considered as a multi-scale work starting from the molecular level micro-kinetics to particle level mass transfer combined with reaction and then moving up to the reactor level involving flow, heat and mass transfer phenomena [13]. Different approaches present in the literature vary according to the purpose of the work and whether it should be examined on a macroscopic level or microscopic level. Conventional approaches include pseudo-homogeneous models and heterogeneous models. Particles are not actually being generated in both approaches. In fact, the porous medium of the packed bed system is modelled with effective parameters rather than actually resolving the packing structure. Thus, local porosity effects and local flow patterns cannot be observed. These models tend to fail especially for systems with low tube-to-particle diameter ratio (N) because the inhomogeneities result in remarkable wall effects, local backflow regions and noticeable gradients in both radial and axial directions [1]. As can be seen in Figure 2.1, there are different heat transfer mechanisms happening in a packed bed system; therefore, effective parameter models may not always adequately describe the heat or mass transfer phenomena in the bed. With the rapid advancement of computational fluid dynamics (CFD) and computational science in recent years, major work has been done on simulations of fluid-solid catalytic interaction in packed bed systems. To overcome the issues in the aforementioned models, 3D particle-resolved CFD modelling strategy which accounts for the actual geometric structure of a particle-filled bed was introduced by the pioneering studies of Dixon et al. [14].

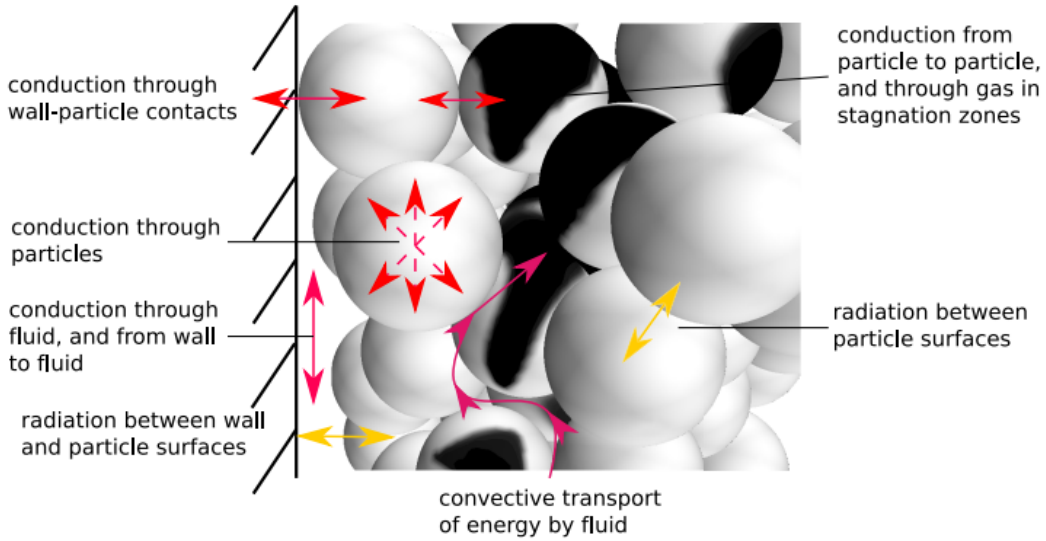

Figure 2.1: Different heat transfer mechanisms present in a packed bed [1], [2].

2.1 Pseudo-homogeneous models

In pseudo-homogeneous models, particles and the fluid phase are assumed to be identical. In other words, there is only one variable representing the packed bed system in terms of heat and mass transfer. A representative temperature and pressure field of pseudo-homogeneous model utilization can be observed in Figure 2.2 where the particles are not shown, but the packed bed is modelled as a lumped homogeneous porous media. Among the pseudo-homogeneous model family, the ideal one-dimensional model can be considered the most basic one. This is the plug flow model in which the gradients of concentration and temperature are present only in the axial direction. Pressure drop is often negligible which allows for the use of a total mean bed pressure for the formulation of this model [15]. Nevertheless, the most common equation for predicting the pressure drop for the flow through packed columns, namely Ergun equation, can be used for the calculations if pressure variations are significant and cannot be neglected for the bed. An extension of this model is applied by taking axial mixing into account with effective medium parameters such as effective diffusivity and effective thermal conductivity. Taylor [16] proposed that the effective diffusivity of species changes by the shear flow due to the combined effect of radial diffusion and convection for large Peclet numbers. Aris [17], then extended the model to a wider

range of Peclet numbers. They then developed a dispersed plug flow model in which they indicate an average axial velocity can be referred for molecules to travel, but the random deviations from ideal plug flow through moving the bed result in an axial mixing to some degree. Thus, they ended up with an equation describing a mean-averaged species concentration to incorporate the different phases as a function of time along the bed where the diffusive term is represented by an effective dispersion coefficient.

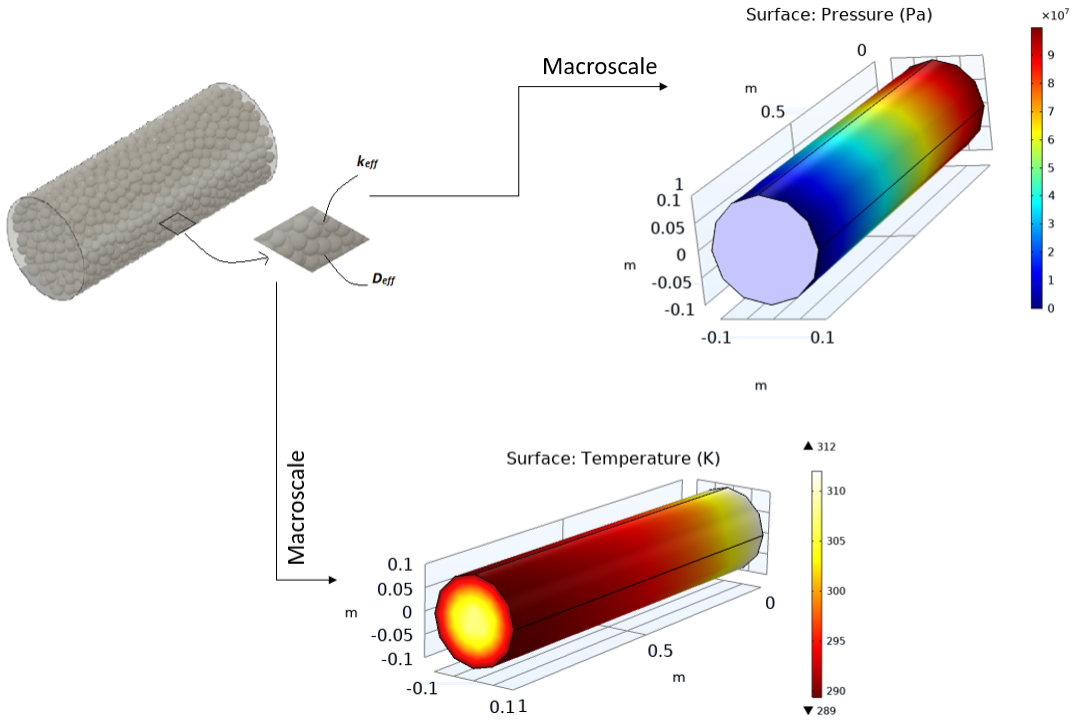

Figure 2.2: Contour plots of pressure and temperature resulting from homogeneous model utilization.

Levenspiel and Bischoff [18] examined the effect of axial dispersion and came up with criteria including physical parameters and Peclet number to neglect the effect of axial dispersion based on the concentration difference at the outlet of the reactor with and without axial dispersion. For adiabatic reactors, Carberry and Wendel [19] stated that for the bed depth surpasses around 100 particle diameters, the influence of axial dispersion of heat and mass upon conversion is insignificant for the flow velocities utilized in industrial applications. In another study, Wakao and Kaguei [20] proposed that the dispersion coefficient is influenced by the fluid phase's molecular diffusivity,

the solid phase's effective diffusivity, as well as the reaction in the particles. For a packed bed experiencing rapid reactions, they find that the dispersion coefficient is twenty times the fluid phase's molecular diffusivity, yet it is only one-fourth the value of the molecular diffusivity.

These models, which have only been briefly discussed, predict uniform temperatures and conversions in a cross-section by excluding the radial resistance to heat and mass transport. In the case of highly exothermic or endothermic reactions involved, this is obviously a serious simplification. A model that forecasts the specific temperature and conversion pattern in the reactor is required for such circumstances [21]. This led to the discussion of radial mixing in these types of packed beds. Researchers developed models to predict an artificial wall heat transfer coefficient to capture the 'jump' near wall region and the effective conductivity and diffusivity based on the radial direction which they express the mixing effects in the continuum model with [22], [23], [24]. Mcguire and Lapidus [25] used an alternative method in which the bed is considered as an assembly of two-dimensional completely mixed cells with two outputs leading to the next row of cells. To consider radial mixing, alternate rows are offset by half a stage. They applied this methodology to non-steady state operations.

The efforts of introducing radial mixing have been developed by the introduction of velocity profiles. Often, the plug flow type of constant and uniform in the radial direction velocity is used with sufficient restrictions. However, to capture the concentration and temperature field accurately, hydrodynamic effects should be included [26]. These types of 'pseudo-' models have gained advancement by integrating radial porosity profiles in addition to accommodating the momentum transfer as well as the heat and mass transfer [27]. They can be considered to have become more sophisticated with the usage of extended Brinkman equations based on a radially varying porosity profile with an effective viscosity [28].

2.2 Heterogeneous models

The presence of the solid particle phase is explicitly taken into account in the heterogeneous models, which is the primary distinction between the pseudo-homogeneous

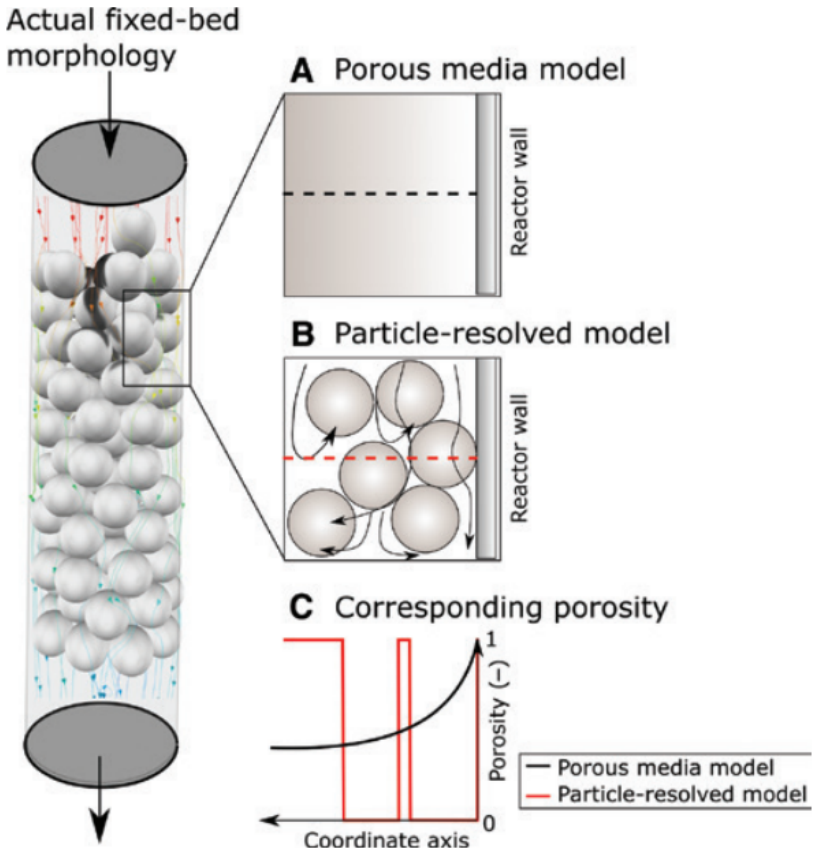

Figure 2.3: Porosity variations in particle-resolved model and porous media model [1].

and heterogeneous models. Even though particles are not actually being generated in the model geometry, governing equations for species transport and heat transfer are solved for two phases simultaneously. Differentiating between conditions in the fluid and on the solid surface or even inside the particle enables us to consider the interfacial, even maybe intraparticle gradients. This type of modelling is essential for such cases as rapid reactions with a significant heat effect in the bed. One-dimensional plug flow model can be applied in this type of modelling without the assumption of equal temperature and concentration of fluid phase and particle surface. Industrial fixed bed systems often have flow velocities so high that the concentration and temperature drop over the film at the particle surface are minimal during steady-state operation. However, one should be careful when making design calculations because this may not be the case for systems involving highly exothermic reactions that interacted with catalysts or deposited on catalyst particles such as catalyst regeneration or catalyst

reoxidation [21]. If the internal heat and mass transfer resistances are substantial for the particles as well as with the external limitations, intraparticle temperature and concentration gradients should also be introduced to model the system competently. The reaction cannot be assumed uniform through the particles for such systems. Calculations can be further simplified by bringing the effectiveness factor concept which transforms the intra-particle distributed parameter equations to a lumped form in [29]. The effectiveness factor (η) is a dimensionless parameter which can be classified as the internal effectiveness factor and overall effectiveness factor. The former was introduced by Thiele [30] and described as the ratio of reaction rate in which the pore diffusion resistance is taken into account to the reaction rate in all active sites at the surface conditions. The latter is the ratio of the observed reaction rate in which external and internal diffusion limitations are taken into account to the rate that would take place if the whole surface of the particle has the bulk concentration without any diffusional limitations [31], [32]. It can be implemented as constant which reduces the computational requirements and can be calculated via an analytical or empirical equation without the necessity of integration of the rate through the bed. However, the implementation of this factor as constant could result in a reactor's concentration and temperature gradients being estimated incorrectly [33].

Xu and Froment employed a one-dimensional model including interparticle and intraparticle gradients by neglecting the radial and axial mixing for heat and mass transfer [34], [35]. They evaluated the intrinsic kinetics and effectiveness factors for steam-methane reforming in an industrial reformer and observed that the effectiveness factors of the two reactions decreased through the reactor length. They also remarked that the reason most researchers obtained activation energies as almost half the amount of the value of intrinsic ones relied on that result. Nevertheless, implementing the effectiveness factor as a variable from particle to bed model results in the loss of computational ease [33]. Thus, the trade-off between precision and computational efficiency should be made accordingly. In fact, the heterogeneous models that introduce fluid and solid phase conservation equations separately and couple the solid phase to the fluid phase explicitly took intraparticle diffusion limitations into account; thus can discard the use of effectiveness factor [33].

The integration of radial mixing similar to the pseudo-homogeneous models has been

considered especially for heat transfer to be incorporated correctly. McGreavy and Cresweell [36] studied two-dimensional heterogeneous model by extending the one-dimensional model that accounts for interparticle and intraparticle gradients with the terms representing radial heat and mass transfer. They assumed that the heat transfer in the radial direction takes place mainly in the fluid phase. However, even for the high velocities present in the industrial systems, the film and solid phase influence the radial heat transfer by at least 25% [24]. Thus, the assumption on radial and axial mixing conditions and the solid and fluid phases' contributions should be made conscientiously for not representing the system roughly.

Heterogeneous models can be further elaborated by concerning the impact of the pore structure of the catalyst particles. Wakao and Smith proposed a micro- and macro-pore model to describe the random pore structure of the catalysts [37]. Many industrial catalysts ended up having larger voids between the pressed materials in the pelleting process in addition to having smaller voids between the intraparticle pores in the pelleting process. Thus the model of Wakao and Smith [37] can be considered a good approximation for the pellets whose pore size distributions are bimodal [38]. Some other models have been proposed to describe the pore structure of the catalysts incorporating the pore size distributions and effective diffusions [39], [40].

2.3 Particle-resolved CFD models

The particle-resolved CFD modelling approach for packed bed systems consists of three main steps. It starts with the packing generation step which can be done by different methodologies. Then, in the second step, the packed bed-generated geometry is meshed to assemble the domain for numerical simulations. In the last step, all of the conservation equations are numerically solved using the developed mesh model. Figure 2.4 shows a representative workflow of the particle-resolved CFD modelling which is divided into subcategories according to the method applied in the steps.

2.3.1 Packing generation

Packing generation can be made by different methods and can have either an idealized arrangement or a random arrangement. In the reconstructive methods, first, image reconstruction of the randomly filled bed is made using experimental tomography output. Imaging techniques such as magnetic resonance imaging (MRI) or X-ray microtomography (XMT) can be used for the surface or volume description whose voxel data of the resulting tomography is converted to [41], [42]. These techniques have also been used as comparison tools for simulation results of packed columns [43], [44].

Packed geometry can also ideally be arranged via a mathematical description of the location of the particles. Regularly placed particles on the domain are of interest in the particle-resolved simulations of packed beds [45], [46], [47]. Periodically re-united lattice unit cells of particles such as simple-cubic, face-centered cubic and body-centered cubic can be used to derive an ideally arranged packed geometry [48], [49]. Dixon et al. [50] demonstrated that a spiral arrangement of layers made up of sphere particles can provide a pseudo-random packing geometry. The segment-type approach is also applied by constructing the stacked particles or representative segments for the sections of bed geometry [51], [52].

Resolving the random packing structure of the packed beds for especially larger scale is not an easy task with scanning and reconstructing with tomographic methods due to its required high computational efforts. Idealized arrangements of packed beds are useful methods to obtain a packed geometry domain relatively easier than the reconstructive methods. However, they are not the actual representation of the randomly packed bed systems for both industrial and laboratory scales even though they can be used to anticipate the random bed extrapolated from the regular bed [53]. Therefore, researchers focused on the computer-generated random packing structure.

The most dominant methods in computer-generated random packing are the Monte Carlo based methods and the Discrete Element Method (DEM). Monte Carlo method is a statistical technique that involves initializing the particles at random in the domain and then statistically moving them in order to either decrease the fraction of voids or

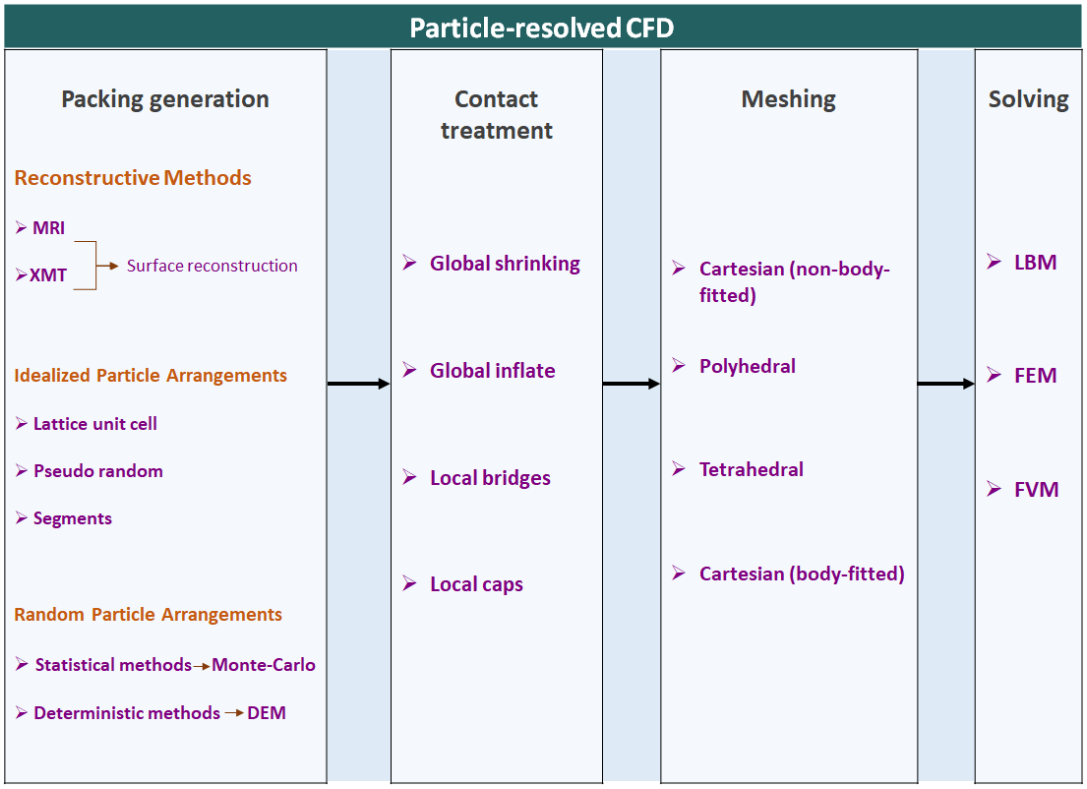

Figure 2.4: General workflow of particle-resolved CFD methodology. Adapted from [1].

minimize overlaps [1]. It is a common method that is used to obtain the random particle arrangement by several researchers [54], [55], [54], [56], [57]. Monte Carlo methods have the disadvantage of not accounting for particle collisions which may result in the unphysical arrangement of particles if they are non-spherical as shown by Caulkin et. al. [58].

While Monte Carlo is a stochastic method having randomized outcomes, DEM is a deterministic method that utilizes contact mechanics derived from discrete particle physics and Newton's law of motion. Discrete Element Method was originally suggested by Cundall and Strack [59] as a discrete numerical model to account for the mechanical behaviour of discs and sphere assemblies. The method is based on the Lagrangian modelling approach and basically applies the equation of motion to the particles. Additionally, contact forces between the particles are included in DEM. Two main discrete simulation approaches are present in DEM frameworks: the hard-sphere model and the soft-sphere model. The former approach assumes the particles

can solely have a momentum exchange by collision and the interaction forces are impulsive. Consequently, explicit consideration of inter-particle forces is not made. This model is applicable to the systems with dilute particle regimes, it must not experience multi-particle contacts for this model to be valid [1]. In the latter approach, particles are allowed to have a slight overlap during the collision in order for interaction forces between particles to be calculated. Different approaches on modelling the contact forces exist on the basis of contact mechanics to correlate the aforementioned overlap during the collision such as the linear model, a non-linear spring-dashpot model such as the simplified no-slip Hertz–Mindlin model and a full Hertz–Mindlin and Deresiewicz model [60].

2.3.2 Meshing

The packed structured geometry obtained by various methods discussed above is required to be spatially discretized by mesh elements with particular interest according to the numerical solver chosen. Although a structured mesh is computationally efficient and less memory demanding than an unstructured mesh, it is not feasible to obtain structured mesh for a packed bed system due to its complex geometry. Cartesian cut-cell meshing is used in Lattice-Boltzmann simulations. For Finite Element Method simulations, usually, tetrahedral and hexahedral meshes are applied whereas for Finite Volume Method simulations tetrahedral, mixed hexahedral, polyhedral or curvilinear structured meshes are at least applicable[1]. Usually, due to unstructured mesh requirements for complex geometry, tetrahedral volume elements are preferred; however, polyhedral volume elements seem to start to be popular among researchers for fixed-bed simulations [61], [62], [63].

The main challenging part of meshing packed structured geometries is the contact points between neighbouring particles and between the particles and the wall. These contact points lead infinitely fine cells in contact zones to avoid skewness in these regions. However, this cannot be achieved by a feasible computational cost. Several researchers investigated this topic and different methodologies are proposed. Figure 2.5 shows different contact modification methodologies that are present in the literature. Global shrinkage method was the first method to overcome this issue in which

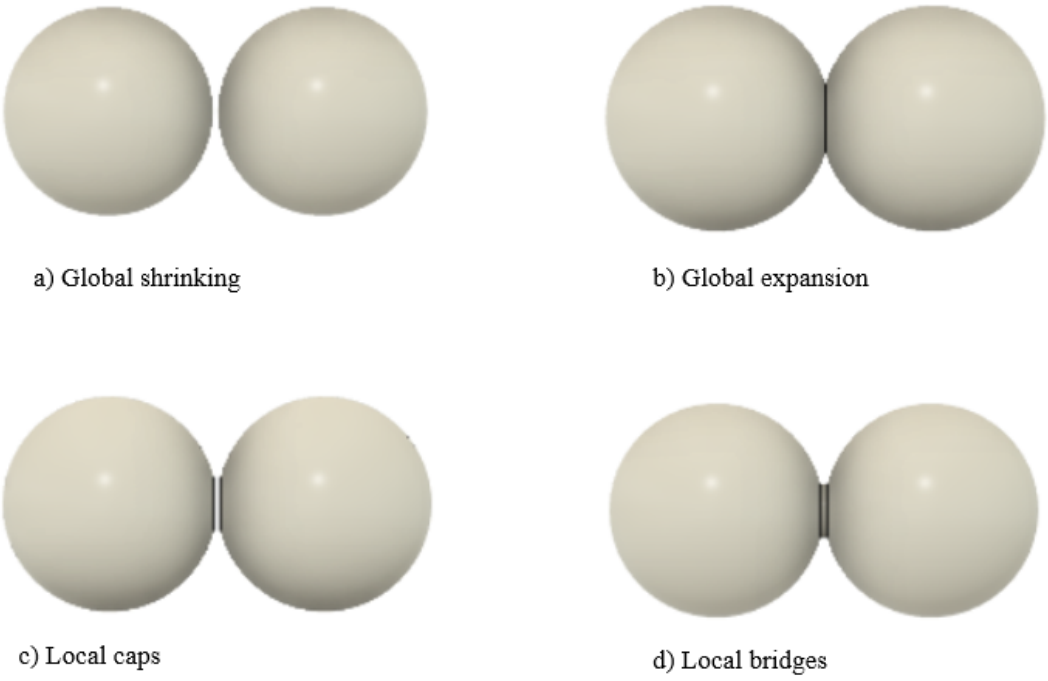

Figure 2.5: Different contact treatment methods.

the particles have been shrunk by a percentage of their actual diameter so that have become not being touched in the contact points and this volume can be meshed with less skewed cells. Global expansion method was also applied [64] in which particles' diameters are increased to a certain extent to replace the contact points with an intersecting volume of particles. Other than shrinking or enlarging the particle diameters, local modifications in the contact zone were studied. Eppinger et al. [63] proposed a local caps method in which the surfaces of the particles in the contact point are flattened to have minimized voids that can be meshed with better-quality cells. On the contrary, Ookawara et al. [65] introduced a method that locates cylindrical bridges between the center of contacting spheres that are after united with the particles before the mesh. All these contact treatment methods were examined by Bu et al. [3] in terms of porosity, flow and heat transfer characteristics. Figure 2.6 shows their representative mesh configurations of different contact point treatment methodologies. They have concluded that the local bridges method is the one that does not violate the actual porosity, resulting in a less significant impact on pressure drop than other methods. According to their study, it also has satisfactory results for predicting the

local heat transfer.

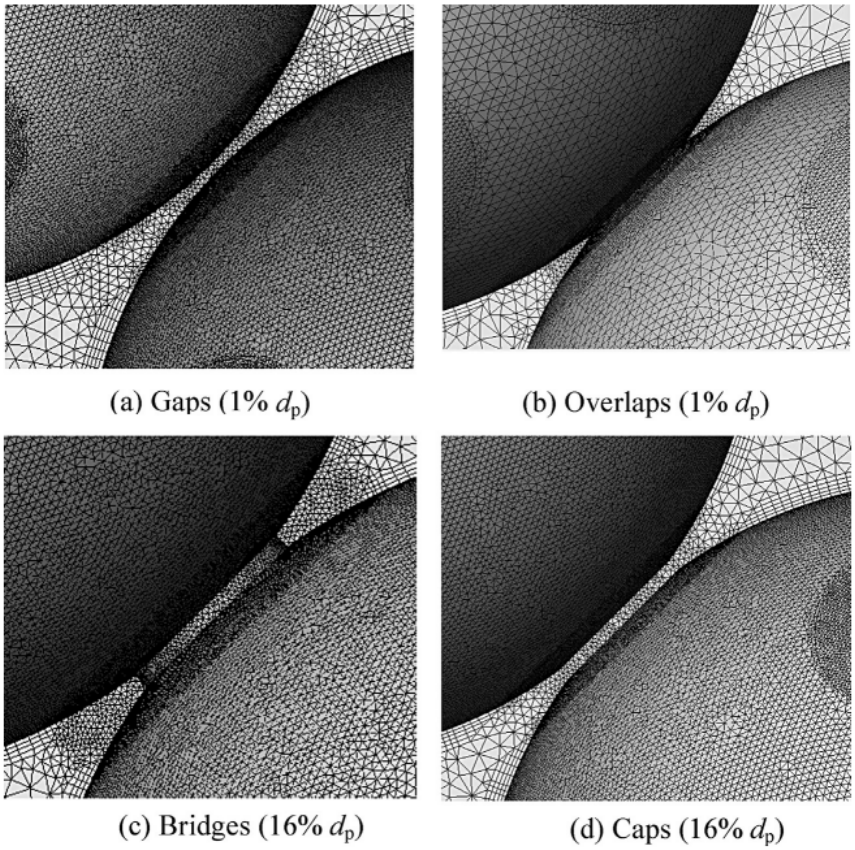

Figure 2.6: Representative meshing study of different contact modification methods [3].

Additionally, studies by Dixon et al. [47] showed that the global methods, in which particles shrunk or enlarged uniformly, changed void fraction so much that produced inaccurate findings for the drag coefficient (C_D). Local approaches that introduce bridges or remove spherical caps exclusively at the sites of contact produce significantly better outcomes for C_D. They have come to the end that the bridge method is preferable for heat transfer since fluid gaps drastically diminish it while particle overlaps greatly enhance it.

2.3.3 Solving

The governing equations for the particle-resolved packed bed are the fundamental equations based on the conservation of mass, momentum, energy and chemical

species i. Conservation of mass and momentum for modelling of laminar flow in the bed is achieved by the Navier-Stokes equations. Turbulence can be modelled with so-called turbulence models: Direct Numerical Simulation (DNS), Large-eddy simulation (LES) and Reynolds-averaged Navier-Stokes simulations (RANS).

In DNS, the time-dependent Navier-Stokes equations are solved without any approximation or averaging on the system-descriptive variables; thus, it is more accurate solution for the solution of turbulent flow fields. However, the computational cost is drastically higher than LES and RANS simulations due to the requirements of resolving the complex range of temporal and spatial scales of turbulent flow. The extremely fine mesh resolution and small time steps required are very challenging for such simulations. The mesh requirements are more flexible in LES since the large turbulent eddies are solved whereas the small ones are modelled with sub-grid scale stresses in the model. However, it is still computationally unpractical due to the transient nature of the model [1]; thus, it is not common among researchers for packed-bed simulations. RANS modelling is more popular in the field because it is less numerically demanding and computationally efficient. No turbulent eddies are solved in RANS simulations because they are modelled via algebraic equations.

Besides modelling flow in packed bed systems, the procedure to solve the energy equation and species transport equation is more straightforward for the interstitial fluid region. The challenging part of solving systems of equations is to incorporate heterogeneous catalysis into these systems. Coupling micro-kinetics with the inter-particle domain has a high computational cost, especially for systems having detailed reaction mechanisms. The complex geometry created as a 3D random packing structure is already computationally expensive due to the large number of cells and as the number of species such as gas phase species and surface adsorbed species increases, it becomes more complicated in terms of computational efficiency. In essence, there are two methods that can be used to shorten the overall time until convergence. Simplification of the mechanism, which includes species and reactions, to a skeletal mechanism or optimization can be used to reduce the cost of the computation of the formulas used in reaction rate computation algorithms. These techniques are frequently referred to as chemical acceleration and were primarily established in the combustion community [66]. Researchers implemented different methodologies that are basically

storage/retrieval techniques to combine the microkinetics with the CFD environment: in-situ adaptive tabulation method (ISAT) [67], cell agglomeration method (CA) [68], the operator splitting algorithm [69], Reaction-diffusion Manifold (REDIM) [70] reduced kinetic model and dynamic adaptive chemistry [71] etc. Detailed examination of these models can be found in [66] and [1].

All the balance equations should be numerically solved by different numerical techniques. Lattice-Boltzmann Method (LBM), Finite Element Method (FEM) and Finite Volume Method (FVM) are the numerical methods that have been used and still are being used by many researchers. FVM is the most used method in particle-resolved CFD studies so far. The reason FVM is the most common in the packed-bed simulation field is linked to its practicality on unstructured meshes and the advancements achieved in automated meshing methods in recent years [1]. FVM is a numerical method that discretizes the numerical domain into a number of finite volumes, commonly referred to as cells, in order to solve the governing equations. Partial differential equations are integrated over each component, converting it into a set of solvable algebraic equations. It is based on the continuity of overall flux, i.e. diffusive and convective fluxes on each cell face. The face values of the variables are calculated via different numerical approximations such as first-order upwind scheme, central differencing scheme, power-law scheme, second-order upwind scheme, etc.

FEM is another numerical method that works by breaking up the domain into a variety of finite elements that are connected at nodes. The end output of FEM is a continuous function consisting of several shape functions, each of which describes how the system behaves in a single element. Although the shape functions can have any specification, they are most frequently utilized with linear or polynomial functions. The nodal points contain the solution to the variables. The benefit of FEM is that it offers a fairly general framework for solving any problem, however; being very memory-demanding makes usage of FEM not as common as FVM simulations [1].

LBM is another method for numerical discretization which is derived primarily from the kinetic theory of gases and the approach has been modified for the macroscopic flows by adapting coarse graining. It is a stochastic approach whose idea is based on simulating fluid flow using stochastic distributions of particles travelling on a regular

discrete lattice. The particles move to a nearby lattice point at each time step and then collide locally to disperse their velocities [72]. LBM is considered to be a faster approach compared to the traditional Navier-Stokes solvers; thus, it has been common over the past decades with the advancements in its computational power. It has also been used in the simulation of packed bed reactors and found to be very efficient for complex structured geometries [73], [74]. However, it also has the disadvantage of being impractical for conjugate heat transfer problems and steady-state problems due to the transient nature of the method.

In this study, the particle-resolved CFD approach was utilized to model the packed adsorption bed to avoid the aforementioned shortcomings of the conventional homogeneous and heterogeneous models. Random local porosity distributions determine the flow pattern for especially low tube-to-particle diameter ratio beds; thus, the aim is to capture that level of complexity having an effect on the heat and mass transfer characteristics for the adsorption bed with ethanol/activated carbon working pair. Most of the studies based on the particle-resolved CFD approach concentrated on heterogeneous catalysis. There are studies for the adsorption-based packed bed systems; however, they are not as common as heterogeneous catalytic systems. Therefore, the study also aims to fill the gap for the adsorption-based packed bed systems. Discrete Element Method was used for the random packing generation due to its accuracy and applicability with the commercial EDEM software. Additionally, the local bridges method was utilized as a contact treatment strategy because of the advantages of representing the local porosity distributions and heat transfer characteristics with less error margin [3]. Unstructured mesh was employed due to the complex nature of the geometry, and a commercial Finite Volume Method software, ANSYS Fluent, was used for the CFD simulations of flow, heat and mass transfer with the adsorption model.

CHAPTER 3

METHODOLOGY

In this study, a randomly packed adsorption bed with ethanol/activated carbon working pair was 3D simulated in terms of flow, heat and mass transport as well as adsorption kinetics. The adsorption bed was aimed to be used in an adsorption heat pump or as a heat storage system; thus, it is more likely for the bed to have a small tube-to-diameter ratio (D/d_p). The rise of bed temperature during adsorption lowers the bed adsorption capacity. To solve this issue and achieve high performances, packed beds with small *N* are implemented providing a faster removal of heat for packed bed sorption processes [75] and heat storage applications [76]. Moreover, hydrodynamics was discovered to have a significant influence on the adsorption efficiency for both laboratory scale and industrial applications [77].

Conventional pseudo-homogeneous and heterogeneous models cannot adequately describe this type of bed since the assumption of continuous porous medium fails due to high porosity near the wall and damped oscillatory trend of radial porosity. The particle-resolved CFD approach allows us to examine this complex flow pattern and interparticle and intraparticle transport phenomena which have a significant impact on overcoming heat and mass transfer limitations. Therefore, this approach is adopted in the modelling of the study. Computer-generated random packing structure of the adsorption bed was obtained. Contact point treatment and mesh generation were carried out. Then, CFD simulations of the bed was conducted. The procedure applied as a whole is described in Figure 3.1.

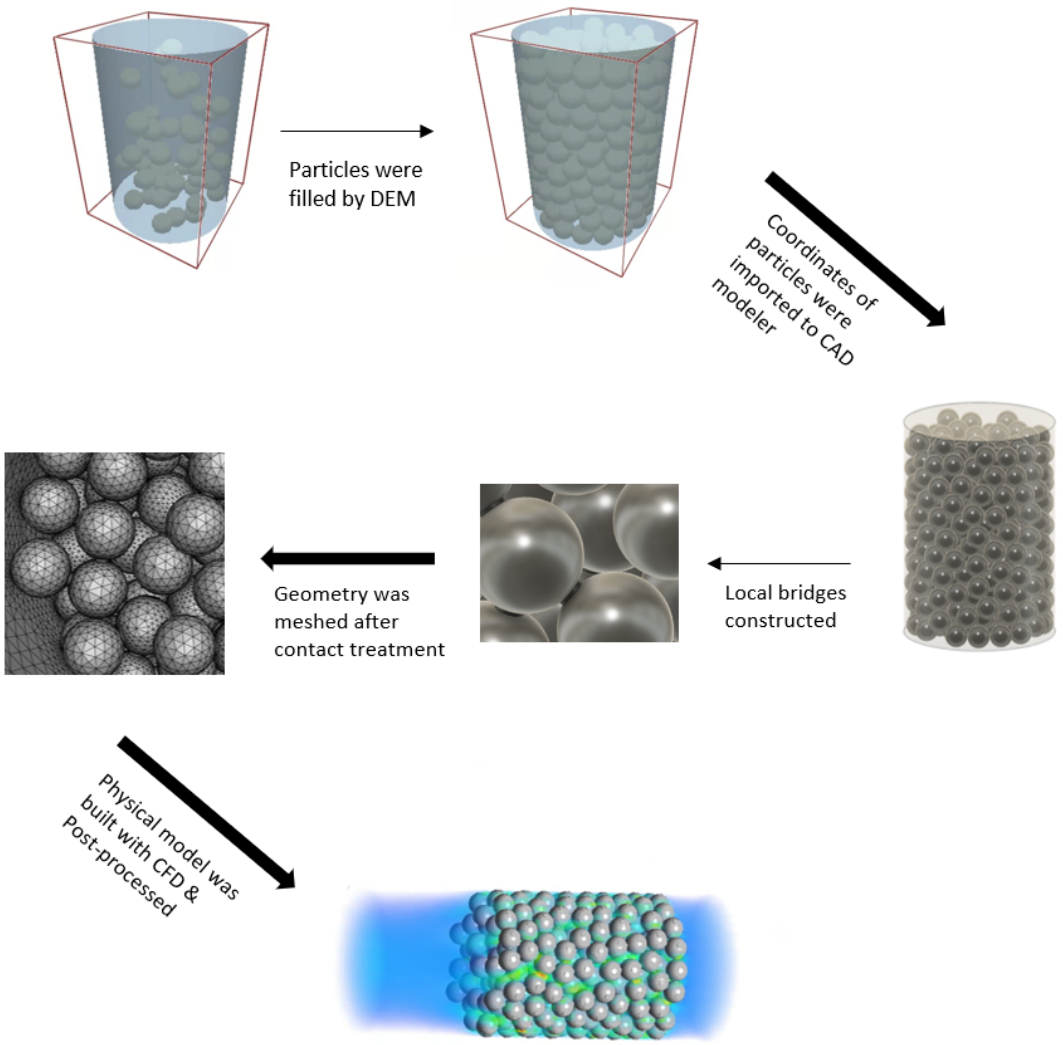

Figure 3.1: Procedure applied in this study to model the randomly packed adsorption bed.

3.1 Packing Generation: Discrete Element Method

Random packing structure of the bed is generated by discrete element method (DEM) using commercial Altair EDEM 2022 software. Discrete element method is a widely applied deterministic method to obtain random particle arrangements for the packed bed systems because it shows good agreement with the experimental data in terms of the actual porosity representation of the bed [78], [79], [80]. Through the idea behind DEM, the contact forces between the cylinder wall and particles as well as

inter-particle contact forces are incorporated in addition to Newton's law of motion in the simulation of the filling process. The soft-sphere model has better accuracy and is the most general method in most DEM packages [4]. Thus, it is applied in the DEM simulation of this study. For the calculation of the interaction forces, the momentum balance on a material particle brings up:

$$m_p \frac{d\vec{v}}{dt} = \vec{F_s} + \vec{F_b} \tag{3.1}$$

where m_p is the mass of the particle, $\vec{v}$ is the particle velocity and $\vec{F_s}$ and $\vec{F_b}$ are the surface forces and body forces, respectively. Forces acting on particle surface are drag force and pressure gradient force whereas body forces are given as:

$$\vec{F_b} = \vec{F_g} + \vec{F_c} \tag{3.2}$$

where $\vec{F_g}$ is the gravitational force and $\vec{F_c}$ are the contact forces. Contact forces are specified as:

$$\vec{F_c} = \sum_{neighbor\,particles} \vec{F_{contact}} + \sum_{neighbor\,walls} \vec{F_{contact}} \tag{3.3}$$

Hertz-Mindlin (no-slip) contact force model is employed in the DEM simulation of this work. It is the default model in Altair EDEM due to its effective and precise calculation [4]. It is a variant of non-linear spring-dashpot contact model with the concept of the Hertz-Mindlin theory.

Figure 3.2 shows the contact vector that connects the center of the particles to the point of contact. The components of the contact force are the normal force that acts perpendicular to the body which exerts the force as can be seen in Figure 3.1 3.2. The tangential component of the contact force is the resulting force of tangential overlap. Herewith, Contact forces between particles are calculated by normal force and tangential force as:

$$\vec{F_c} = \vec{F_n} + \vec{F_t} \tag{3.4}$$

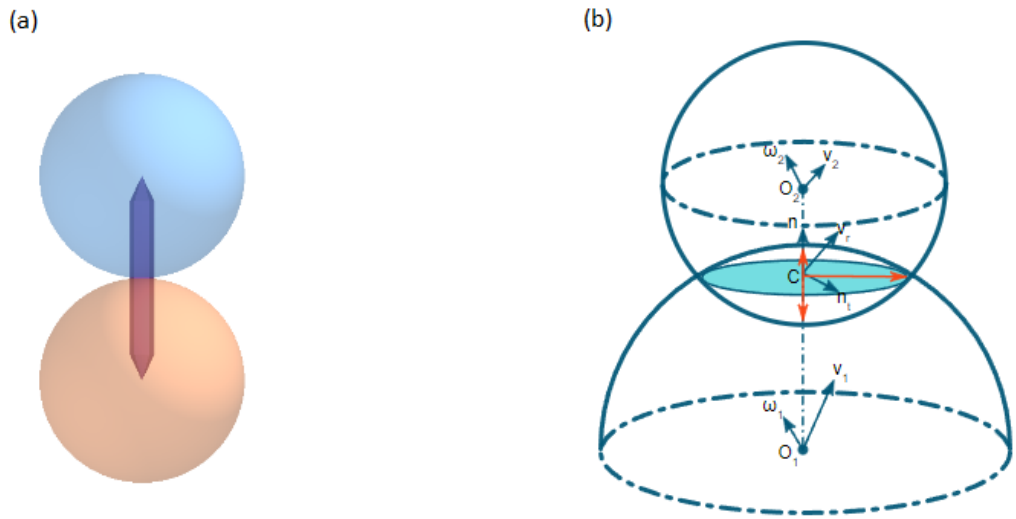

Figure 3.2: (a) Contact vector between two spheres and (b) Components of contact force at the point of contact. [4]

The normal force component is calculated as:

$$\vec{F}_n = \frac{4}{3} E^* \sqrt{R^*} \delta_n^{3/2} \tag{3.5}$$

where E^* is the equivalent Young's Modulus, R^* equivalent radius and δ_n is the overlap in the normal direction. E^* is calculated via Young's Moduli of sphere *i* (E_i) and *j* (E_j) and Poisson's ratios of sphere *i* (ν_i) and *j* (ν_j);

$$\frac{1}{E^*} = \frac{(1-\nu_i^2)}{E_i} + \frac{(1-\nu_j^2)}{E_j} \tag{3.6}$$

Equivalent radius R^* is calculated using the radii of sphere *i* (R_i) and *j* (R_j);

$$\frac{1}{R} = \frac{1}{R_i} + \frac{1}{R_j} \tag{3.7}$$

Similarly, equivalent mass of particles m^* is as function of masses of spheres *i* (R_i) and *j* (R_j);

$$m^* = (\frac{1}{m_i} + \frac{1}{m_j})^{-1} \tag{3.8}$$

β as a function of the coefficient of restitution, e is given as:

$$\beta = \frac{-lne}{\sqrt{ln^2e + \pi^2}} \tag{3.9}$$

The normal stiffness, S_n is defined as:

$$S_n = 2E^*\sqrt{R^*\delta_n} \tag{3.10}$$

The tangential force, $\vec{F_t}$, is dependent on the tangential overlap δ_t and the tangential stiffness S_t:

$$\vec{F_t} = -S_t\delta_t \tag{3.11}$$

with

$$S_t = 8G^*\sqrt{R^*\delta_n} \tag{3.12}$$

where G^* is the equivalent Shear modulus. Tangential damping is additionally defined as:

$$\vec{F_t^d} = -2\sqrt{\frac{5}{6}}\beta\sqrt{S_t m^*}\vec{v_t^{rel}} \tag{3.13}$$

where the relative tangential velocity is denoted by $\vec{v_t^{rel}}$. With μ_s being the coefficient of static friction, the tangential force is limited by the Coulomb friction $\mu_s F_n$.

Material and interaction parameters are specified in Table 3.3. Some parameters cannot be explicitly obtained for the activated carbon particles such as friction coefficients; therefore, the input parameters of DEM simulation are adjusted according to the parameters in [65] which are set for the catalytically active particles.

Table 3.1: Parameter values used in DEM simulation

Run			Values
particle diameter	d_p	m	0.002
tube diameter	D	m	0.014
shear modulus	G	Pa	$2x10^8$
Poisson's ratio	v	-	0.23
coefficient of restitution	e	-	0.94
coefficient of static friction	μ_s	-	10^{-6} - 0.2
coefficient of rolling friction	μ_r	-	1/100

Spherical particles having a diameter of 2 mm were sent to the cylindrical container bed to fall naturally by gravity in DEM modelling. Figure 3.3 shows the steps of DEM simulation for the particle filling process.

3.2 Meshing

Once we obtain the randomly packed cylindrical bed with mono-sized spherical particles by DEM, we have the coordinates of each sphere in the cylindrical domain. These coordinates were imported to the CAD software Autodesk Fusion 360 to create the geometry of random spherical particles. Spherical particles were generated from these coordinates and the inlet and outlet sections of the cylindrical tube were extended to ensure uniformity at the inlet and prevent backflow at the outlet. As discussed in the Literature Review 3.2, the local bridges method was found to be preferable in terms of representing the flow and heat transfer characteristics of the packed bed by not over or underestimating the porosity. As a result, the local bridges method was chosen as a contact treatment strategy in this work. In the programming interface of Autodesk Fusion 360, the packed spheres geometry was built with local bridges using Python programming language. A certain threshold is determined and cylindrical bridges were constructed between the particles whose closest distance between adjacent particles is below this threshold. Similar treatment is given to the area where the particle and tube wall come into contact. The bridge diameter was set

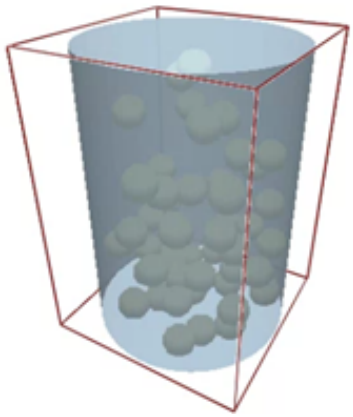

(a) t = 0.01 s

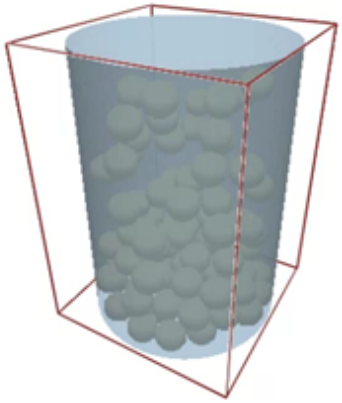

(b) t = 0.02 s

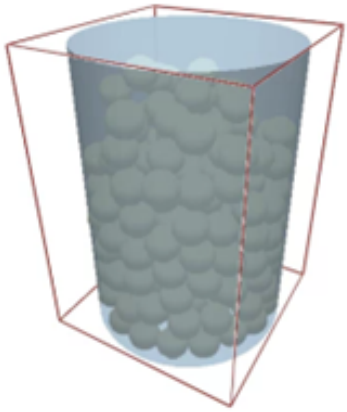

(c) t = 0.05 s

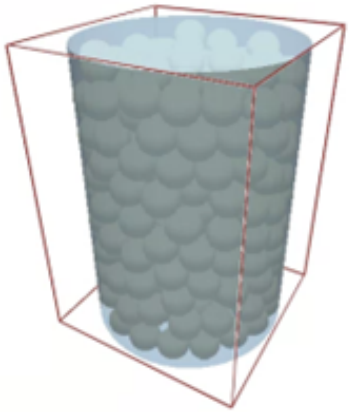

(d) t = 1 s

Figure 3.3: DEM simulation of particle filling process of the bed

as 25 $\%$ of the sphere diameter in accordance with the recommendation of Louw et al. [81]. They recommended that the bridge diameter should be higher than 0.2 of particle diameter in order not to have extremely fine cells and should not be higher than 0.3 of particle diameter since porosity error drastically increases above $0.3d_p$.

The resulting CAD geometry was imported to a commercial pre-processor Ansys ICEM CFD software. Unstructured mesh generation was applied since it is more suitable for complex geometries. Firstly, Octree algorithm was applied for the volume mesh and then the existing mesh is used for Delaunay mesh and tetrahedral volume elements were generated. We can see the skewed cells before the contact treatment in Figure 3.4 and the better quality mesh after the bridge generation.

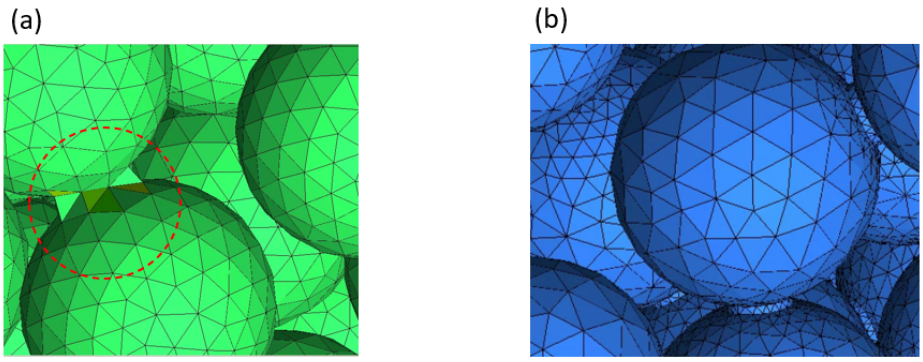

Figure 3.4: (a) Skewed cells near contact region before the contact treatment, (b) Bridged cells near contact region

Mesh independency study was carried out with three different grids: Grid 1, Grid2 and Grid 3. Grid 1 is coarser than the mesh developed for this study and has 1737009 cells, whereas Grid 3 is finer than the mesh developed for the study, having 11704283 cells. Grid 2, which has 4675643 cells, was selected after the grid independence study.

Transient outlet temperature, mass fraction and velocity data were compared for three grids. Figure 3.5 shows the mixed-cup temperature profiles of the bed for different grids. It can be observed that the temperature profiles are almost identical differing

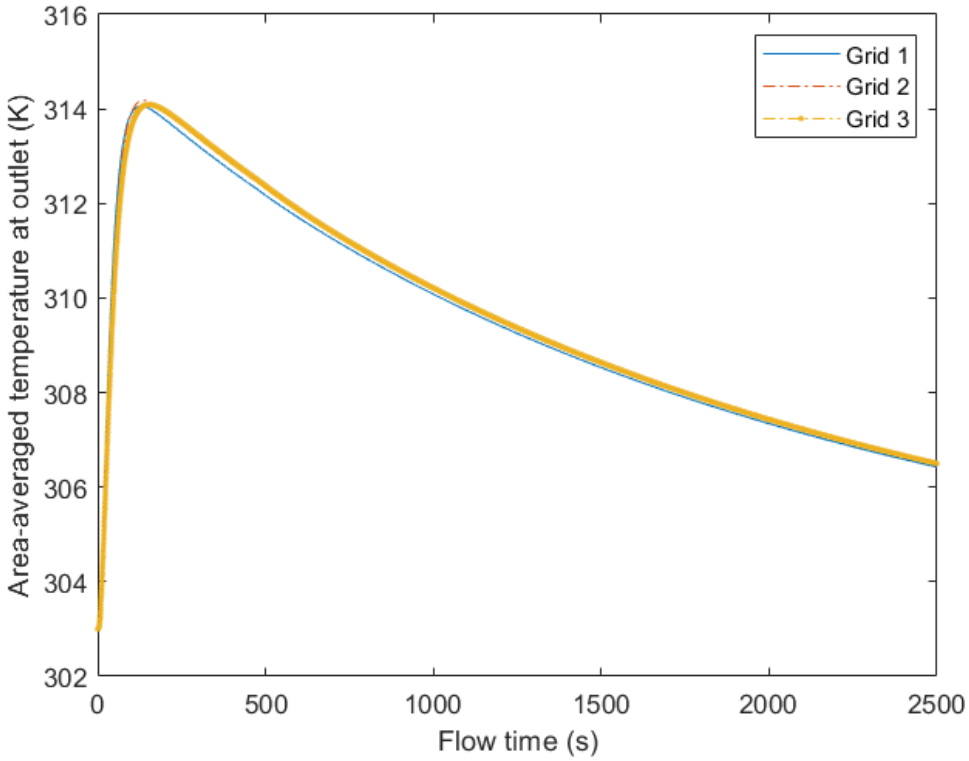

Figure 3.5: Outlet temperature profiles of different grids.

in the peak temperatures by ≈ 0.1 %. Outlet mass fraction of C_2H_5OH and velocity profiles, as well as the pressure drop along the bed for different grids as a function of time are given in the Appendix section.

3.3 CFD simulations

CFD simulations of the developed mesh model were performed using commercial CFD software Ansys Fluent R2021 which is based on Finite Volume Method. Several user-defined functions (UDF), which can be seen in Appendix C, were used to customize the model according to our system specifications for boundary conditions, source terms and physical properties.

Model description and boundary conditions were given in Figure 3.6. Fluid domain consists of a gas mixture of inert (N_2) and ethanol vapor whereas the solid domain consists of porous activated carbon particles. A constant inlet velocity, temperature

and mass fraction of ethanol were given for the inlet boundary conditions. The outlet was set to 'pressure-outlet' boundary condition at atmospheric pressure. The wall was treated as adiabatic and 'no-slip' boundary condition was applied for the wall of cylinder and wall of particles. 'Coupled' boundary condition for applied for energy and flux continuity was applied for the mass transfer which will be given in the following. SIMPLE scheme in Fluent was set for pressure-velocity coupling. Second order upwind scheme was set for momentum, energy and species, whereas first-order upwind was applied for turbulent k and ϵ. After some test runs having all the numerical discretization schemes as second-order upwind, no significant differences were observed in bed temperature, adsorbed amount of ethanol or averaged quantities of k and epsilon. Thus, turbulence quantities were run with first-order upwind in order to decrease the computational cost. First-order implicit method was used for the transient formulation in a pressure-based solver. Default convergence criteria of Fluent which is scaled residuals of 10^{-6} for energy and 10^{-3} for all the other equations were set by monitoring the solution with the averaged bed temperature and adsorbed amount.

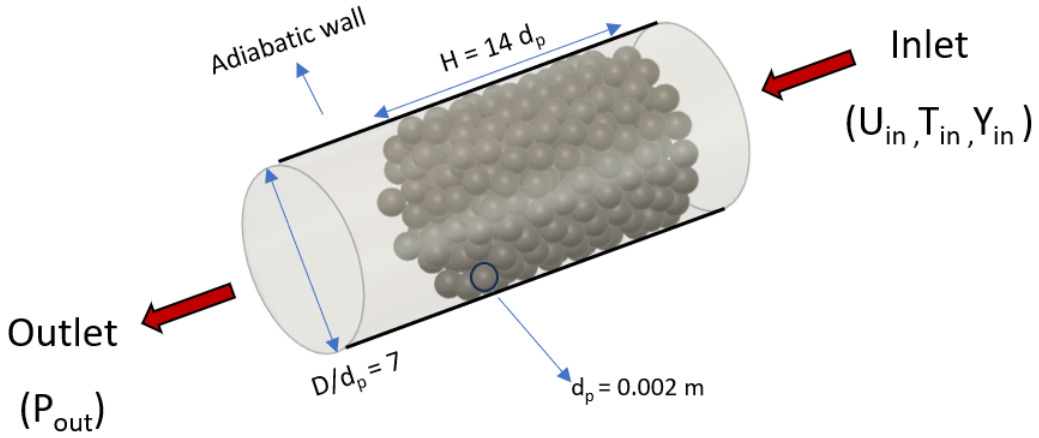

Figure 3.6: A representative scheme for the model domain with boundary conditions.

3.3.1 Governing equations for interparticle fluid domain

Continuity equation and conservation of momentum equation are given as:

$$\frac{\partial \rho}{\partial t} + \nabla \cdot (\rho \vec{v}) = 0 \tag{3.14}$$

$$\frac{\partial}{\partial t}(\rho \vec{v}) + \nabla \cdot (\rho \vec{v} \vec{v}) = -\nabla p + \nabla \cdot \bar{\bar{\tau}} \tag{3.15}$$

$$\bar{\bar{\tau}} = (\mu + \mu_t)[(\nabla \vec{v} + \nabla \vec{v}^T) - \frac{2}{3} \nabla \cdot \vec{v} I] \tag{3.16}$$

where ρ is the density, $\vec{v}$ is the velocity vector, and p stands for pressure, $\bar{\bar{\tau}}$ for stress tensor, μ for molecular viscosity, and μ_t for eddy viscosity, the latter of which is calculated by adding k and ϵ as follows: turbulent k-ϵ model:

$$\frac{\partial}{\partial t}(\rho k) + \nabla \cdot (\rho k \vec{v}) = \nabla \cdot (\mu + \frac{\mu_t}{\sigma_t} \nabla k) + G_k + \rho \epsilon \tag{3.17}$$

$$\frac{\partial}{\partial t}(\rho \epsilon) + \nabla \cdot (\rho \epsilon \vec{v}) = \nabla \cdot (\mu + \frac{\mu_t}{\sigma_t} \nabla \epsilon) + \frac{\epsilon}{k}(C_{1\epsilon} G_k - C_{2\epsilon} \rho \epsilon) \tag{3.18}$$

$$\mu_t = \rho C_\mu \frac{k^2}{\epsilon} \tag{3.19}$$

The model constants were set as default in Fluent as:

$C_{1\epsilon}$ = 1.44, $C_{2\epsilon}$ = 1.92, $C_{2\epsilon}$ = 0.09, σ_k = 1.0, σ_ϵ = 1.3 which are taken from [82].

The flow regime in the packed bed systems is determined by the particle Reynolds number which is given as:

$$Re_p = \frac{\rho_f \, v_0 \, d_p}{\mu \, (1 - \epsilon)} \tag{3.20}$$

where ρ_f is the density of fluid, v_0 is the inlet superficial velocity, d_p is the particle diameter and ϵ is the porosity of the porous medium. Dybbs et. al. [83] studied wide

range of particle Reynolds numbers to observe the flow regimes in porous media. They resulted that for the region Re_p<1, viscous, creeping flow occurs and for the region 1<Re_p<10, flow is steady, laminar and inertial in which the pressure drop is not a linear function of the velocity. Transition occurs approximately Re_p=100. Taking these outcomes into consideration, flow in the simulations was modelled with turbulence and wall functions since Re_p>10 in the simulations which is not in the range of pure viscous laminar flow.

Energy equation is applied as:

$$\frac{\partial}{\partial t}(\rho_f h_f - p - \frac{\rho_f \vec{v}^2}{2}) + \nabla(\vec{v} \cdot (\rho_f h_f + \frac{\rho_f \vec{v}^2}{2})) = \nabla \cdot (k_f \cdot \nabla T) \tag{3.21}$$

where h_f is the enthalpy of the fluid, T is the temperature, k_f is the thermal conductivity of the fluid. Enthalpy is calculated via:

$$h = \int_{T_{ref}}^{T} C_p \, dT \tag{3.22}$$

where C_p is the specific heat capacity and T_{ref} is the reference temperature taken as 298.15 K.

Mixture model was used for the calculation of specific heat capacity:

$$C_p = \sum_i Y_i C_{p,i} \tag{3.23}$$

Species transport model is:

$$\frac{\partial}{\partial t}(\rho Y_i) + \nabla \cdot (\rho \vec{v} Y_i) = -\nabla \vec{J_i} \tag{3.24}$$

where the composition-dependent gas density can be calculated via ideal gas as:

$$\rho = \frac{p}{RT \sum_i \frac{Y_i}{MW_i}} \tag{3.25}$$

The diffusion flux of species i in turbulent flow is calculated via:

$$\nabla \vec{J_i} = -\nabla(\rho D_{i,m} + \frac{\mu_t}{Sc_t}\nabla Y_i) \tag{3.26}$$

where μ_t is the turbulent viscosity and Sc_t is the turbulent Schmidt number. Mass diffusion coefficient $D_{i,m}$ is calculated using Fuller-Schettler-Giddings equation [84]:

$$D_{i,m} = 0.001\frac{T^{1.75}(M_A^-1 + M_B^-1)^{0.5}}{p\,(V_A^-1/3 + V_B^-1/3)^2} \tag{3.27}$$

where M_A and M_B are the molar masses whereas V_A and V_B are the diffusion molar volumes of C_2H_5OH and N_2, respectively.

Physical properties of fluid domain is given in Table 3.2.

Table 3.2: Physical properties of fluid domain

Property	Unit	Values
C_{p,C_2H_50H}	J/kgK	2407
C_{p,N_2}	J/kgK	$979.043 + 0.4179T - 0.00117T^2 + 1.674x10^-6$
μ	Pa.s	$1.72x10^{-5}$
k_f	W/mK	0.0454
V_A	[-]	50.6
V_B	[-]	17.9

3.3.2 Governing equations for intraparticle solid domain

The activated carbon particles are modelled as lumped porous medium with uniform porosity. Thus, the energy equation for porous carbon particles is:

$$\frac{\partial}{\partial t}(\epsilon_p\rho_f h_f + (1-\epsilon_p)\rho_s h_s) = \nabla.(k_{eff,s}.\nabla T) + \frac{(1-\epsilon_p)}{\epsilon_p}\frac{\rho_s}{MW}\frac{\partial w}{\partial t}\Delta H_{ads} \tag{3.28}$$

where ϵ_p is the porosity of the particle, h_s is the enthalpy of solid, $k_{eff,s}$ is the effective thermal conductivity of porous particles. The last term on the right-hand side is the source term resulting from the adsorption rate and heat of adsorption which is given as:

$$\Delta H_{ads} = 30 + 0.057\,T(K)\ kJ/mol \tag{3.29}$$

Species transport in the particle domain can be expressed as:

$$\frac{d(\rho Y_i)}{dt} + \frac{(1-\epsilon_p)\rho_s}{\epsilon_p}\frac{\partial w}{\partial t} = -\nabla(-\rho D_{eff,knud}\nabla Y_i) \tag{3.30}$$

The second term on the left-hand side is the source term resulting from the adsorption rate. The composition-dependent gas density can be calculated via ideal gas as:

$$\rho = \frac{p}{RT\sum_i \frac{Y_i}{MW_i}} \tag{3.31}$$

The Knudsen diffusivity for the activated-carbon particle is calculated as:

$$D_{Knud} = \frac{d_{pore}}{3}\sqrt{\frac{8RT}{\pi MW_i}} \tag{3.32}$$

where d_{pore} is the pore diameter of activated carbon particles and MW is the molecular weight of ethanol.

The source terms in the above equations are the adsorption rate expression taken from [85]. Based on Linear Friving Force adsorption model, rate expression was derived by Yurtsever et al. [85] as:

$$\frac{dw}{dt} = k_s a_v (W - w) \tag{3.33}$$

The term $k_s a_v$ depends on the temperature and follows Arrhenius type relationship as:

$$k_s a_v = 0.58\, exp(\frac{-1970}{T}) \tag{3.34}$$

In Eq. (3.33), w is the the adsorbed amount of ethanol (kg C_2H_5OH/kg activated carbon) and W is the adsorption equilibrium capacity depending on T and P_s:

$$W = W_0 exp(-D(Tln\frac{P_s}{P_i})^n) \tag{3.35}$$

where

W_0: 0.3955

D: 0.0006049

n: 1.156

Saturation pressure of ethanol is calculated using Antoine equation:

$$log_{10}^{P_s} = A - \frac{B}{C - T} \tag{3.36}$$

where the constants of Antoine equation are [86]:

A: 5.24677

B: 1598.673

C: -46.424

3.3.3 Particle-fluid interface

The fluxes of species and energy across the particle-fluid interface are both crucial for defining the boundary conditions there and are of great curiosity. In order to maintain continuity, energy and species fluxes should be equal on the fluid side and solid side of the interface. Murthy et al. [87] developed a numerical derivation of

Table 3.3: Physical properties of particle domain

Property	Unit	Values
ϵ_p	[-]	0.35
$C_{p,s}$	J/kgK	700
$k_{eff,s}$	W/mK	0.65
ρ_s	kg/m^3	750
d_{pore}	[nm]	4

heat conduction flux across a boundary of a conjugate solid-fluid heat transfer for finite volume scheme. Dixon et al. [5] extended this formulation for diffusive flux of an arbitrary scalar over a conjugate boundary. The following formula approximates the diffusive flux of a scalar (ϕ) to a wall boundary:

$$J_f \cdot \vec{A} = \Gamma_f \frac{\phi_1 - \phi_0}{ds} \frac{\vec{A} \cdot \vec{A}}{\vec{A} \cdot \vec{e_s}} + S_f \tag{3.37}$$

where (ϕ_0) is the value of scalar at cell C_0 and (ϕ_1) is the value of scalar at cell C_1. The term Γ_f here is the face diffusion coefficient and S_f is the cross diffusion term. Figure 3.7 shows the geometric representation of the terms derived in the formulation. The derivation brings up a face value of an arbitrary scalar at the interface (ϕ_f) as:

$$\phi_f = \frac{h_1\phi_1 + h_0\phi_0}{h_1 + h_0} - \frac{S_0 + S_1}{h_1 + h_0} \tag{3.38}$$

where

$$h_0 = \frac{\Gamma_0}{ds_0} \frac{\vec{A} \cdot \vec{A}}{\vec{A} \cdot \vec{e_{s0}}} \quad h_1 = \frac{\Gamma_1}{ds_1} \frac{\vec{A} \cdot \vec{A}}{\vec{A} \cdot \vec{e_{s1}}} \tag{3.39}$$

This formulation and the geometric representation were adapted in this study to provide a flux continuity of species at the particle-fluid interface as:

$$\rho D_{i,m} \nabla Y_i|_{fluid} = \rho D_{eff,knud} \nabla Y_i|_{solid} \tag{3.40}$$

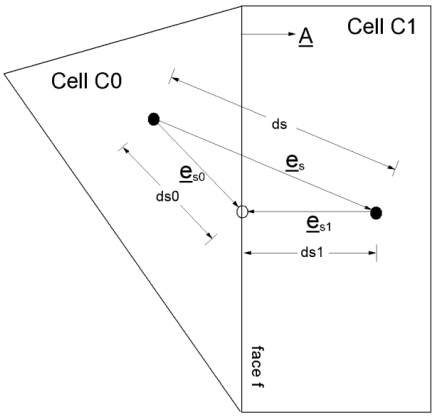

Figure 3.7: Schematic notation of conjugate boundary [5]

This brings up the following face value of species mass fraction Y_i at the interface:

$$Y_{i,f} = \frac{h_1 Y_{i1} + h_0 Y_{i0}}{h_1 + h_0} \tag{3.41}$$

where

$$h_0 = \frac{D_{eff,knud}}{ds_0} \frac{\vec{A} \cdot \vec{A}}{\vec{A} \cdot \vec{e_{s0}}} \tag{3.42}$$

$$h_1 = -\frac{D_{i,m}}{ds_1} \frac{\vec{A} \cdot \vec{A}}{\vec{A} \cdot \vec{e_{s1}}} \tag{3.43}$$

The adaptation of above formulation can be schematically shown for our work in Figure 3.8. Cross diffusion terms are neglected due to isotropic diffusion and orthogonality as was done in [5]. Here, cell C_0 is at the solid side of the boundary and cell C_1 is at the fluid side of the boundary. Y_{i0} is the species mass fraction at the solid side and Y_{i1} is at the fluid side. Vector $\vec{e_{s0}}$ is the unit vector that connects the cell centroid of C_0 to face centroid whereas $\vec{e_{s1}}$ is the unit vector that connects cell centroid of C_1. d_{s0} and d_{s1} are the respective distances.

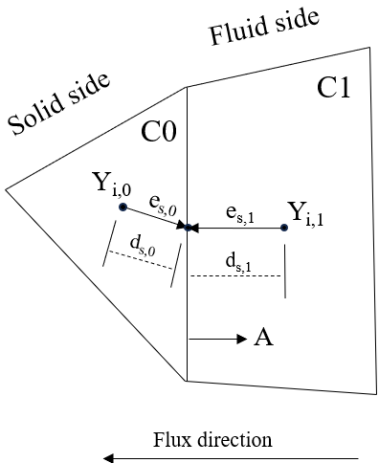

Figure 3.8: Schematic representation of adapted conjugated boundary

CHAPTER 4

RESULTS AND DISCUSSION

In this study, a theoretical and computational model was developed for a random-packing structured ethanol-activated carbon adsorption bed. 3D random packing structure of the bed was obtained by Discrete Element Method simulations using commercial EDEM software. Then, the geometry was meshed in ICEM CFD pre-processor and CFD simulations for the transport phenomena of the bed were carried out using ANSYS Fluent software. Multiscale modelling of the bed was performed based on continuity, momentum, energy equations and adsorption model. Interparticle transport and intraparticle transport phenomena were investigated assuming mainly diffusion and adsorption occur in the intraparticle region. Continuity and momentum equations in the interparticle region were solved using Reynolds-averaged-Navier-Stokes equations with $k - \epsilon$ model with standard wall functions in Fluent. In this section, first, hydrodynamic characteristics of the randomly packed geometry will be investigated. Then, the adsorption-desorption cycles at different temperatures will be examined.

4.1 Hydrodynamic characteristics of the bed

Highly three-dimensional flow can be observed on normalized velocity (v_z/v_{in}) can be observed in the midplanes in Figure 4.1 for different inlet velocities. The velocity reaches almost 10 times of inlet velocity for low Re_p flow and almost 7 times of inlet velocity for high Re_p in some regions. These hotspot velocity regions occur due the non-uniform velocity distribution which may also lead to channeling in the bed. The highest normalized velocity regions observed in low Re_p flow are larger

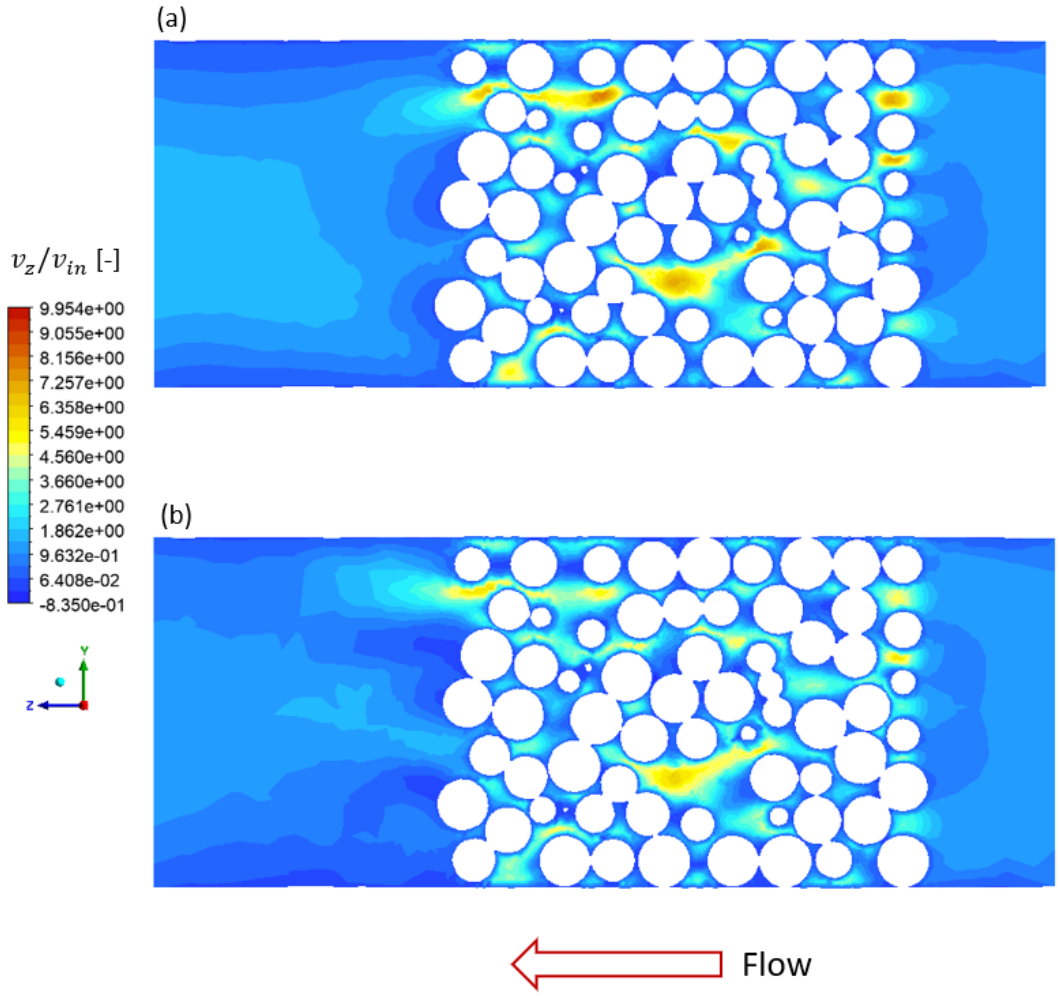

Figure 4.1: Normalized axial velocity contour for an axial plane at x = 0 (a) v_{in} = 0.05 m/s, $Re_p = 12$ (b) $v_{in} = 0.05$ m/s, $Re_p = 120$.

compared to high Re_p flow. This can be explained by the non-axial components and backflow regions are more dominant in high Re_p flow as it becomes more chaotic with increasing velocity. Stagnant zones and regions with negative velocities can be observed as occupying more area in Figure 4.1 (b) than 4.1 (a).

Pressure distribution along the bed is shown in Figure 4.2 for different inlet velocities. As expected, higher velocity resulted in higher pressure drop. Moreover, pressure distribution can be considered as a function of axial direction as Figure 4.2 depicts. Even though local variations can be observed due to voidage distribution, pressure slightly changes in the radial direction.

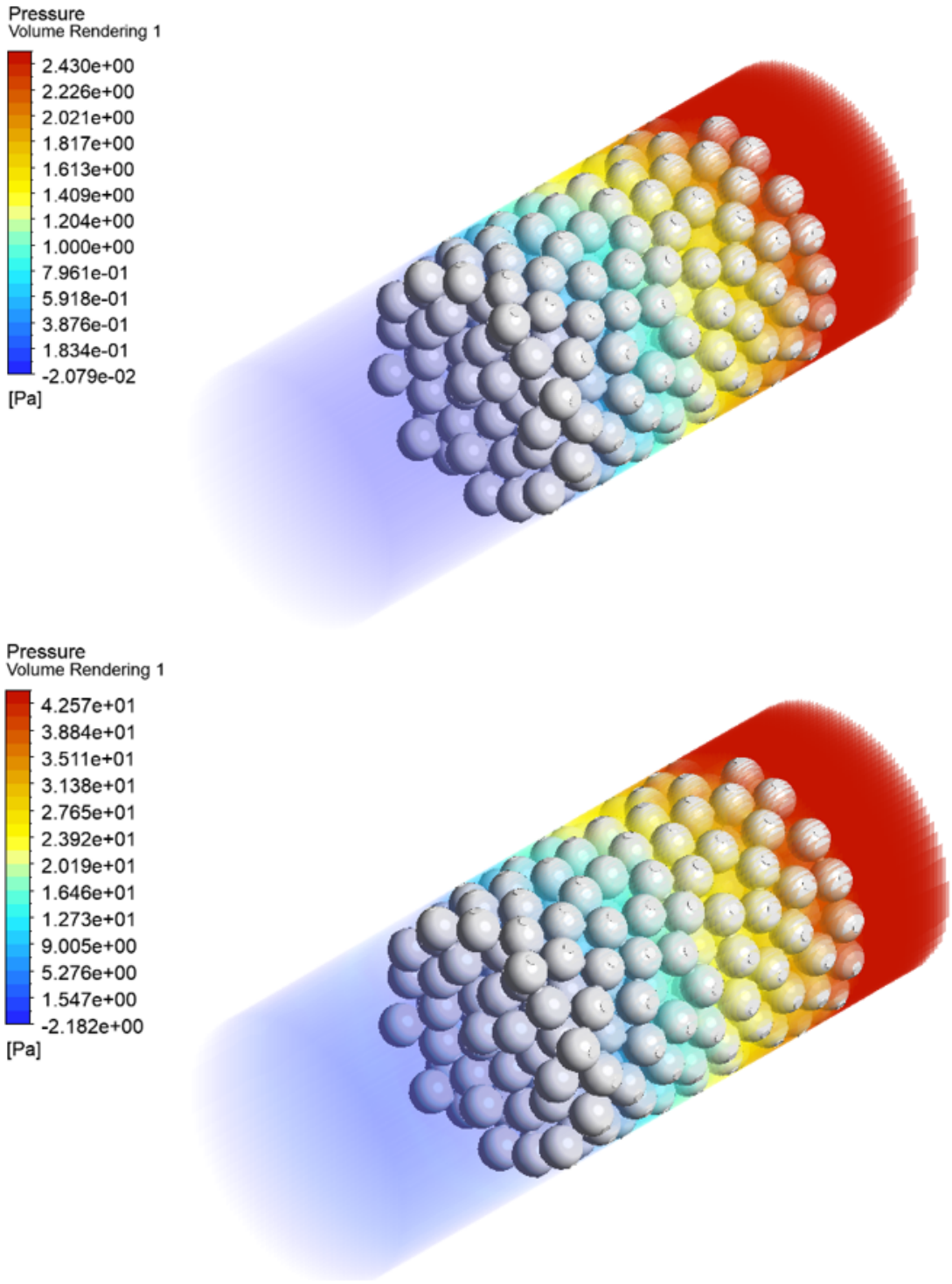

Figure 4.2: Static pressure volume rendering along the bed for (a) $v_{in} = 0.05$ m/s, $Re_p = 12$ (b) $v_{in} = 0.05$ m/s, $Re_p = 120$.

The simulations for adsorption-desorption cycles were performed with 0.05 m/s inlet velocity; thus the following flow characteristics results are given for indicated condi-

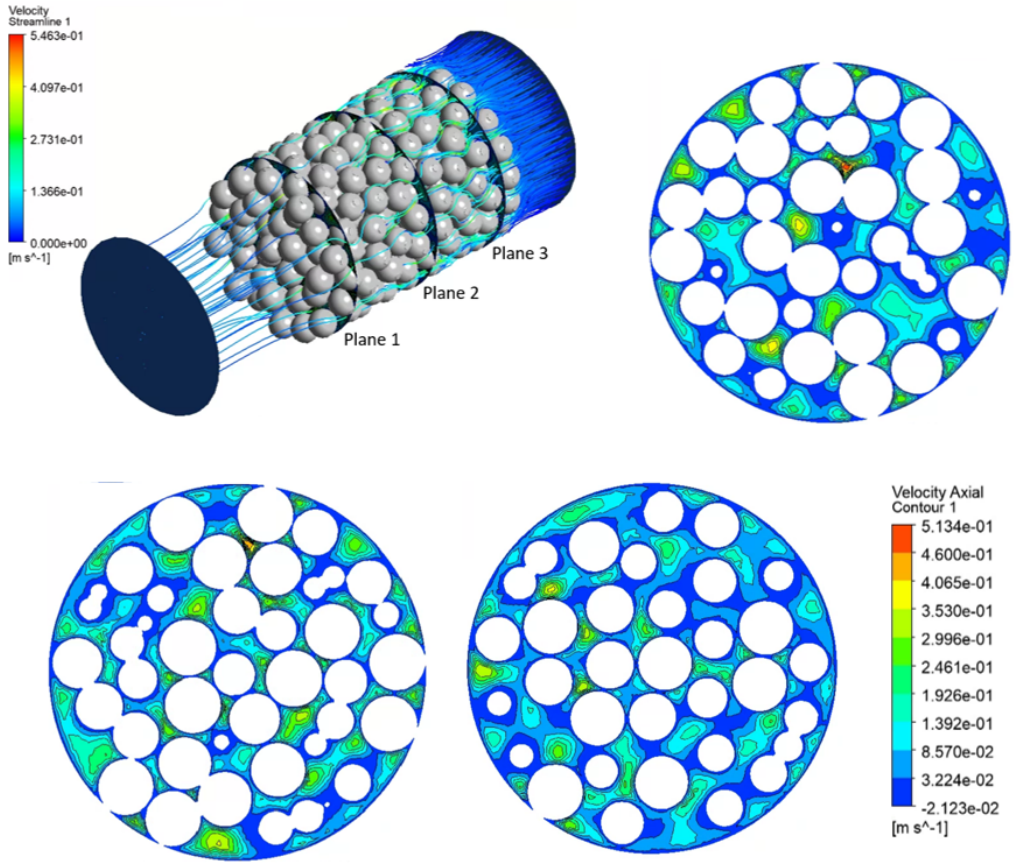

Figure 4.3: Velocity streamlines along the bed and axial velocity distributions in different placed radial planes.

tions. Figure 4.3 shows the velocity streamlines along the bed and the axial velocity distributions of radial planes which are placed at different positions at z = 0. The contour plots of axial velocity exhibit remarkable inhomogeneity in different section planes of the reactor. The overall bed porosity is 0.467; thus the average velocity with the inlet superficial velocity of 0.05 m/s is 0.1 m/s. However, local packing patterns affect the distribution as it reaches almost 3 times the average velocity, even 5 times for some regions.

There are numerous vortexes in the spaces between particles and between particles and the wall, as can be seen from the velocity vector in Figure 4.4. The intricate packing structures, which have a substantial impact on how well fixed-bed reactors work in terms of heat and mass transfer, are what determine these flow parameters. 3D particle-resolved models allow us to examine these regions without the assumption of

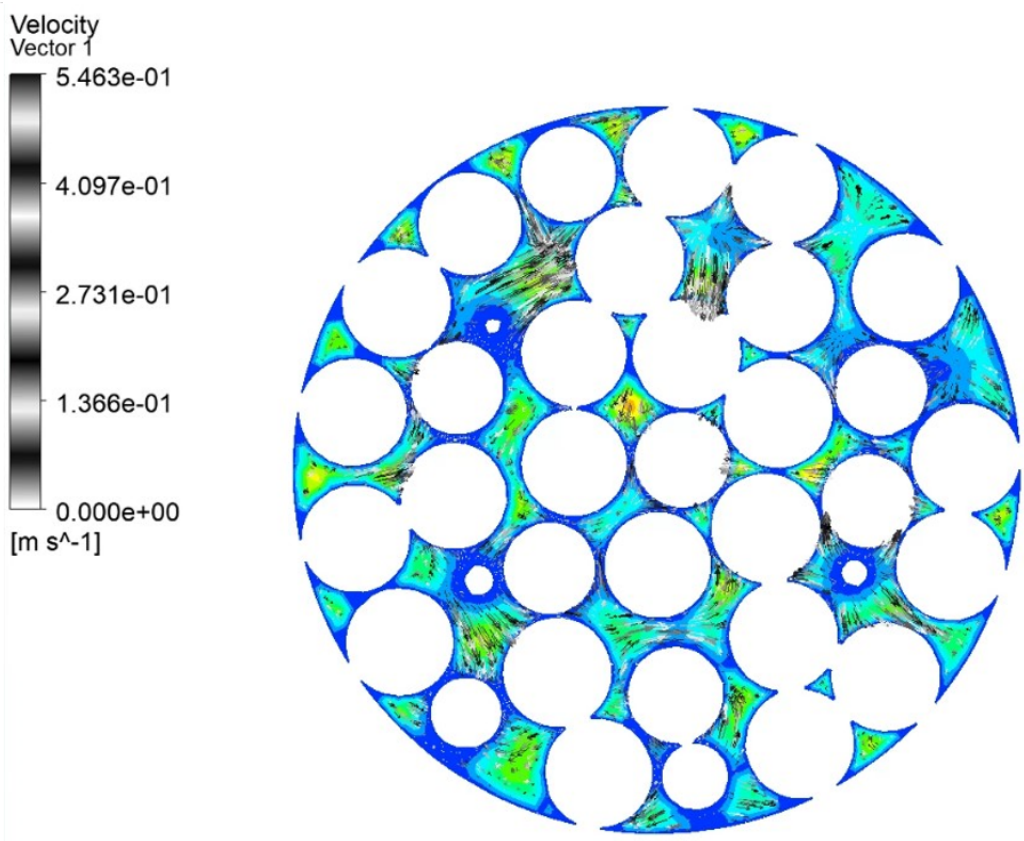

Figure 4.4: (a) Velocity vector and contour at an arbitrary radial plane.

uniform porosity and average velocity along the bed. Stagnant zones and regions with negative velocity, i.e. backflow can also be observed.

As mentioned, the average velocity with respect to inlet velocity is around 0.1 m/s for the bed; however, the isosurfaces in Figure 4.5 depicts that a velocity of 0.25 m/s, which is 2.5 times of the calculated average velocity, occupies a significant area in the interstitial fluid region that is away from the assumption of uniform average axial velocity in the bed.

The histograms of axial and radial velocities in the radial plane at z=0 were given in the Appendix section to demonstrate the distribution of these velocities and observe how close they are to the average velocity in these regions.

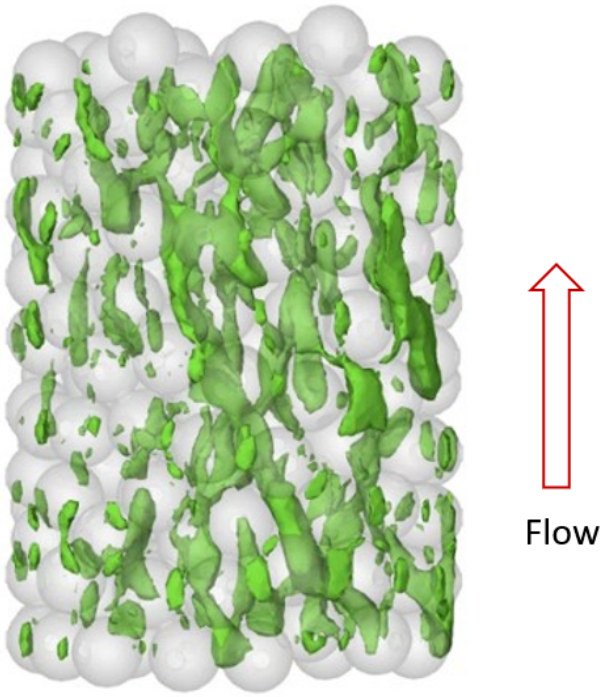

Figure 4.5: Isosurface velocity of 0.25 m/s.

4.2 Adsorption-desorption characteristics of the bed

The start-up of the reactor was in the conditions of already flowing inert (N_2) in the bed with no ethanol vapor. At time equal to zero, a step mass fraction of 0.08, which corresponds to a mole fraction of 0.05, was given at the inlet of the reactor. Initially, system was at 30°C and the inflow temperature is also 30°C for 30°C cycle operation. The same conditions were applied for 60°C cycle operation differing in the temperature being 60°C initially and at the inflow.

The contour plots in Figure 4.6 shows the ethanol mass fraction profile along the bed during the start-up. After the ethanol was sent to the system, it starts to diffuse in the interparticle and intraparticle region and adsorption starts where the ethanol was exposed to the particle. Interparticle diffusion is faster than intraparticle as expected; however, not only the slower diffusion affect the concentration distribution. It is also affected by the adsorption that causes immediate consumption of the ethanol; therefore, interrupts the diffusion of species into the particle.

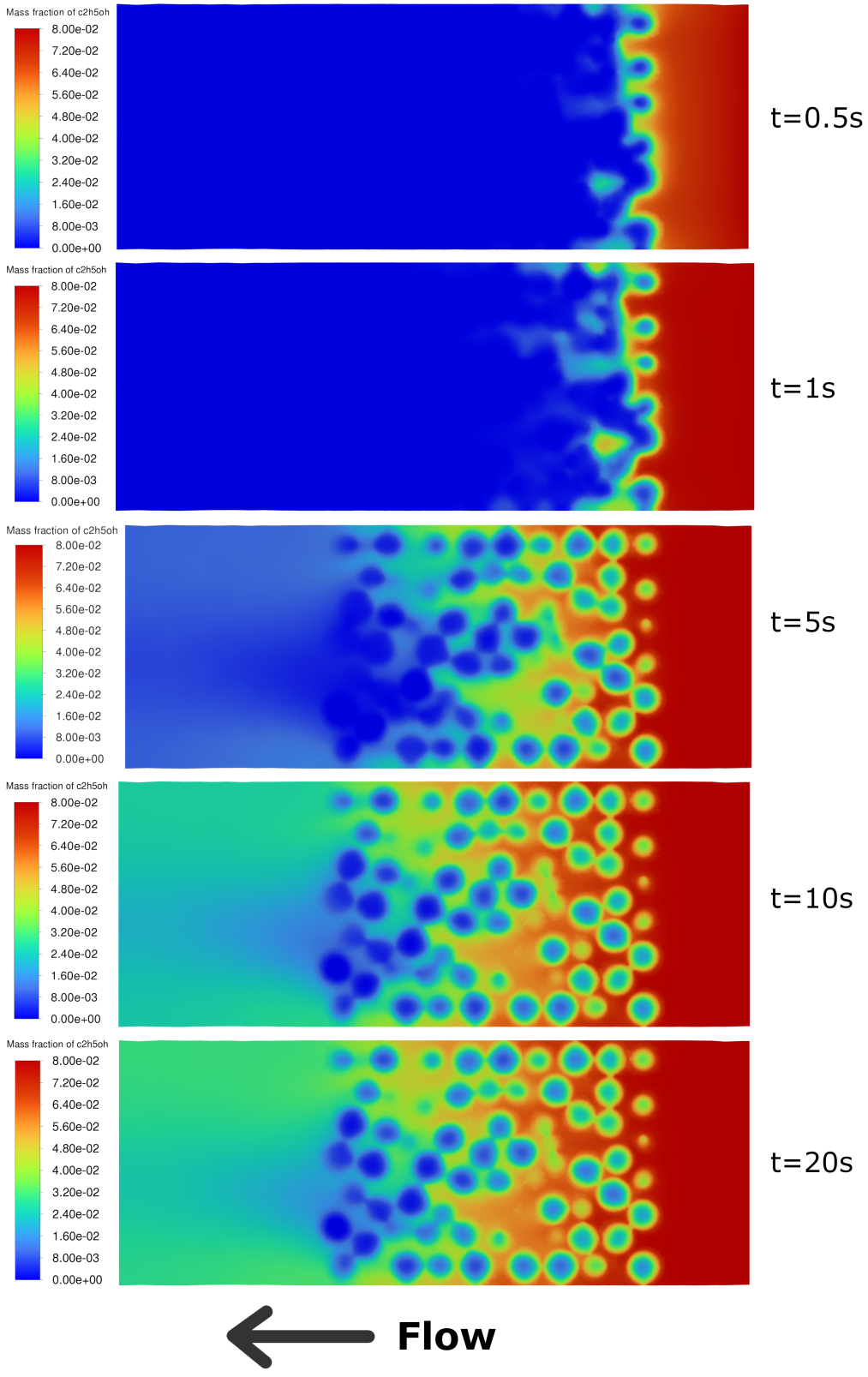

Figure 4.6: Mass fraction contours of ethanol along the bed at the mid-plane (x=0) during start-up at 30°C.

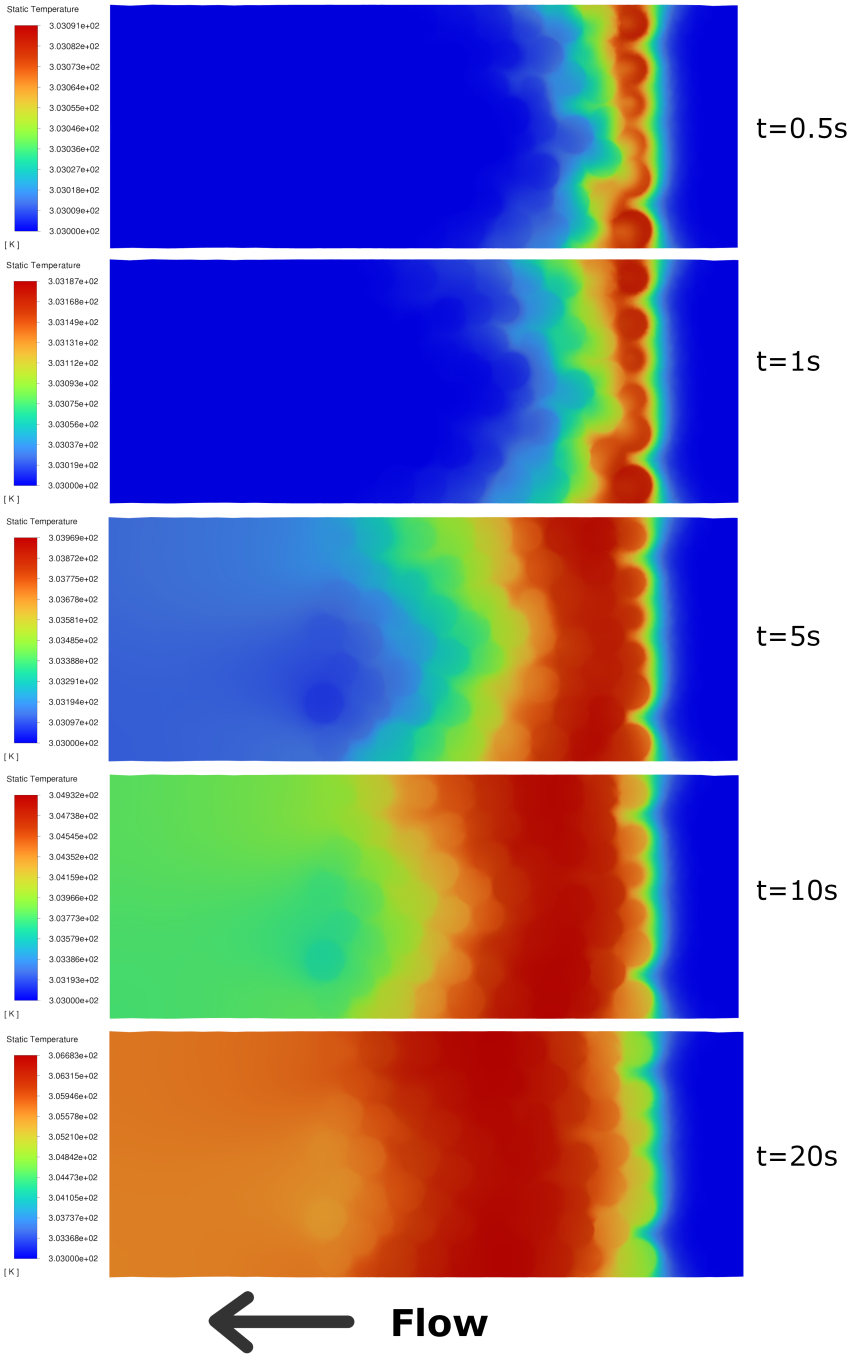

Figure 4.7: Temperature contours along the bed at the mid-plane (x=0) during start-up at 30°C.

Complex packing pattern additionally affects the interstitial regions as shown in Figure 4.6. The region with less void downstream of the reactor has shown to have less concentration of ethanol indicating the interparticle mass transfer limitation around that region.

Figure 4.7 reflects the aforementioned phenomena with temperature distribution being high in the region of the first layer of particles. At time equals 0.5 and 1 s, the ethanol was present only on the surface of the particle where the adsorption immediately started and resulted in the increase of temperature. However, the increase in temperature is also a result of conduction because there is no ethanol inside of particles in some regions but the temperature still increases as time goes by. Although the wall boundary condition is adiabatic, a slight radial temperature profile can be observed in the transient simulation of the bed because of the bypass of flow near the wall where the porosity is high due to random packing. Similarly, the regions with dense packing at the down part of the reactor have less amount of free ethanol; thus, resulting in less generated adsorption heat there.

In Figure 4.8, the adsorbed amounts of ethanol (kg C_2H_5OH/kg activated carbon) in the particles were given at different times for 30°C and 60°C. Since the adsorption rate is faster in low temperatures, w increases with a higher in rate at 30°C than at 60°C as noticeable in the figure. In addition, the already described part in Figure 4.6 which has a closely packed group of particles appeared to have less amount of adsorbed ethanol in both 30°C and 60°C because of the low concentration of free ethanol vapor in that region.

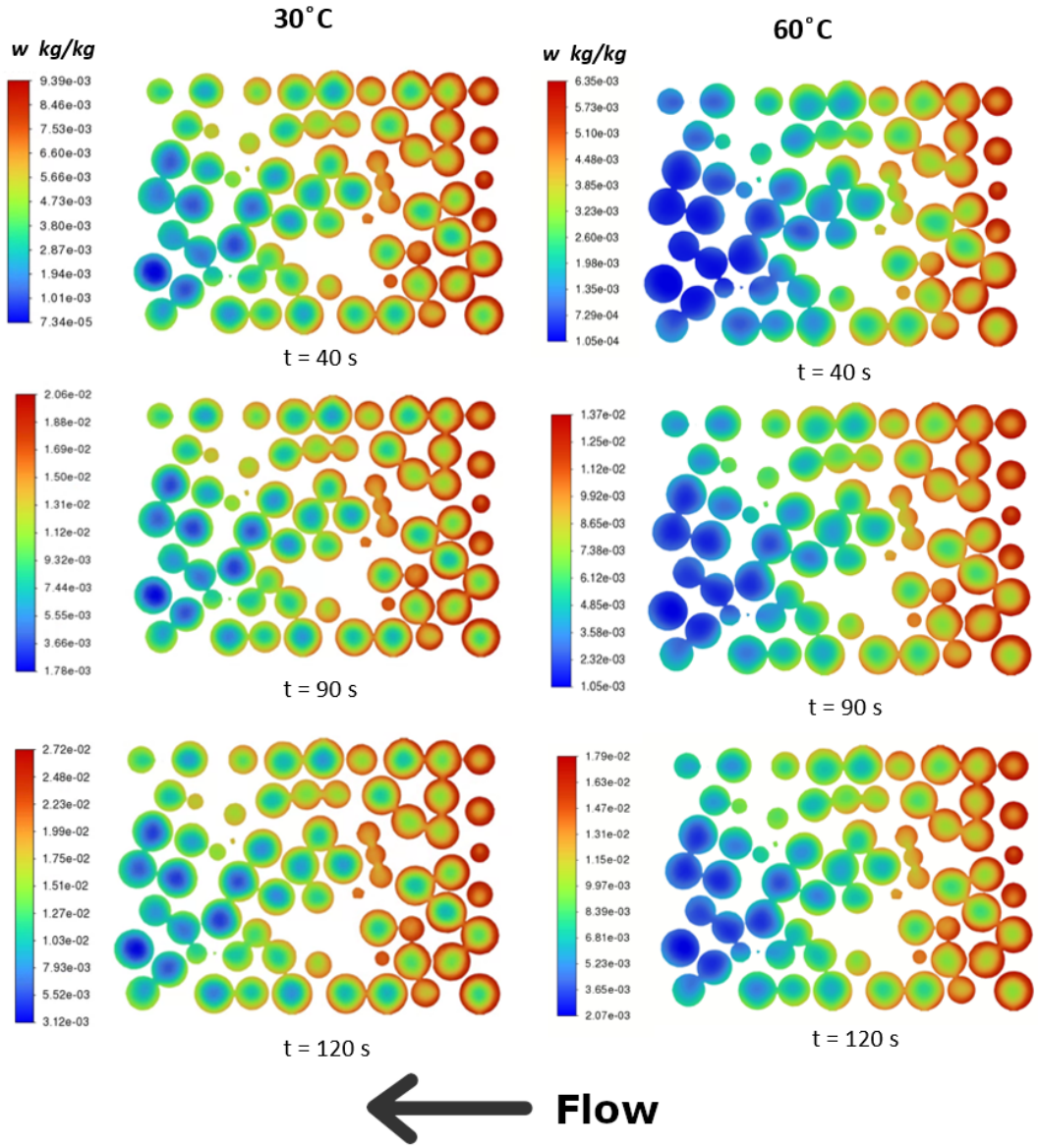

Figure 4.8: Amount adsorbed w (kg C_2H_5OH/kg activated carbon) contours along the bed at the mid-plane (x=0) at different times for 30°C and 60°C.

The adsorption-desorption cycle was performed by giving a step mass fraction of ethanol at the inlet at a time equal to 0, and then giving a step mass fraction of 0.08 corresponding to a mole fraction of 0.05, at the time equal to 4000 s and 6000 s for 30°C and 60°C, respectively. Figure 4.9 shows the step inlet condition where the flow rates drop to 0 at the inlet at the time equal to 4000 s and 6000 s. The outlet mass flow rate of ethanol decreases right away with the feed shut off, then this decrease rate gradually lowers with the desorption having started. A similar trend was observed in 4.10 with a lower rate of decrease in outlet mass flow rate of ethanol due to higher desorption rate resulted in an increase in the amount of desorbed vapor in comparison to 30 °C.

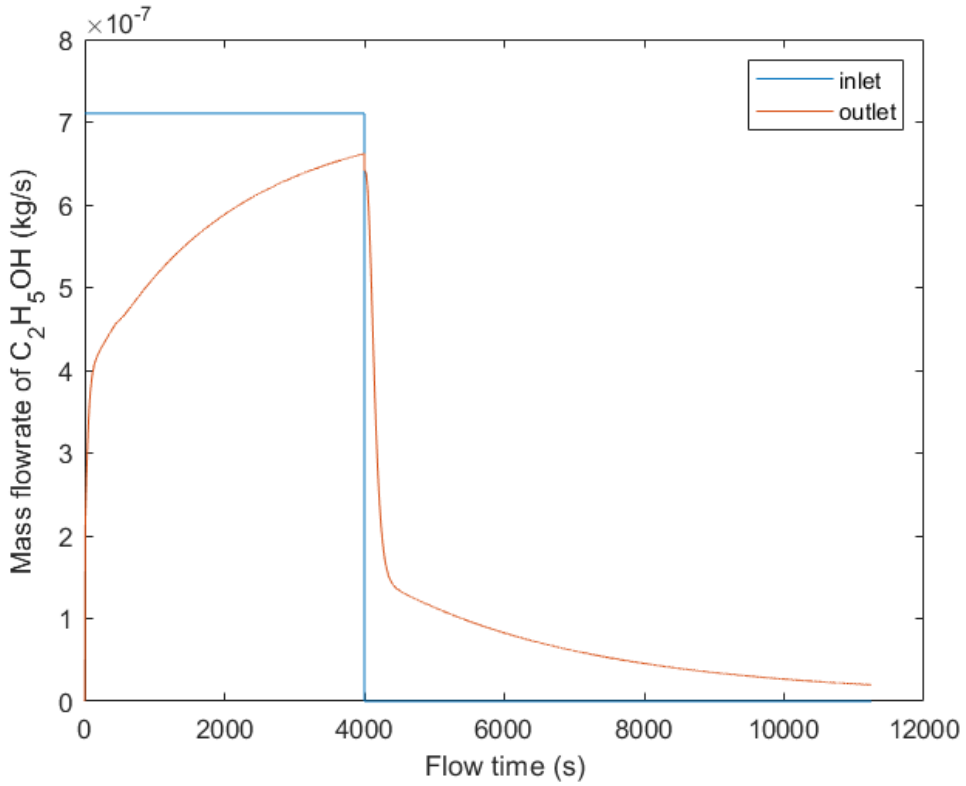

Figure 4.9: Mass flowrates of ethanol at the inlet and outlet surfaces during adsorption-desorption cycle at 30°C.

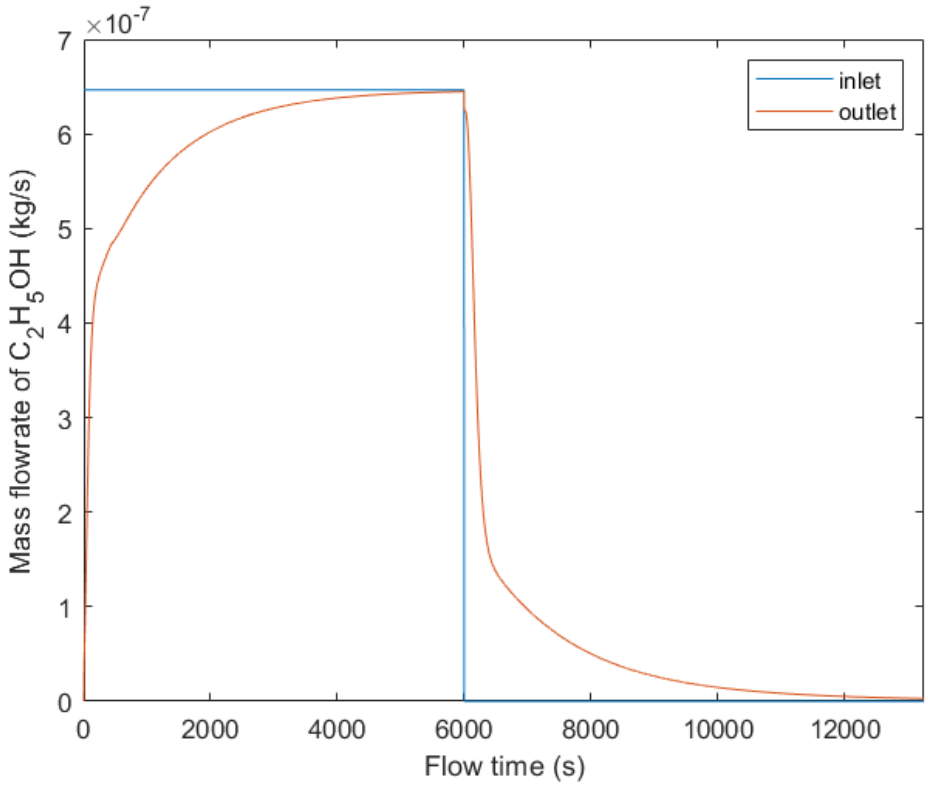

Figure 4.10: Mass flowrates of ethanol at the inlet and outlet surfaces during adsorption-desorption cycle at 60°C.

Figure 4.11 illustrates the profiles of the mass fraction of ethanol and temperature of the bed 60 s after desorption stage starts. After the ethanol in the feed was shut off, desorption starts first in the region with saturated amount of adsorbed vapor, that is, the region closer to the inlet of the reactor. Then, with the inert (N_2) flowing in the bed drives away the desorbed vapor in addition to the diffusion mechanism of the desorbed vapor. Temperature of the bed started to decrease with the start of desorption near the inlet region. As Figure 4.11 demonstrates, the cooling effect is higher in the 60 °C operation due to having higher desorption rate in the higher temperature.

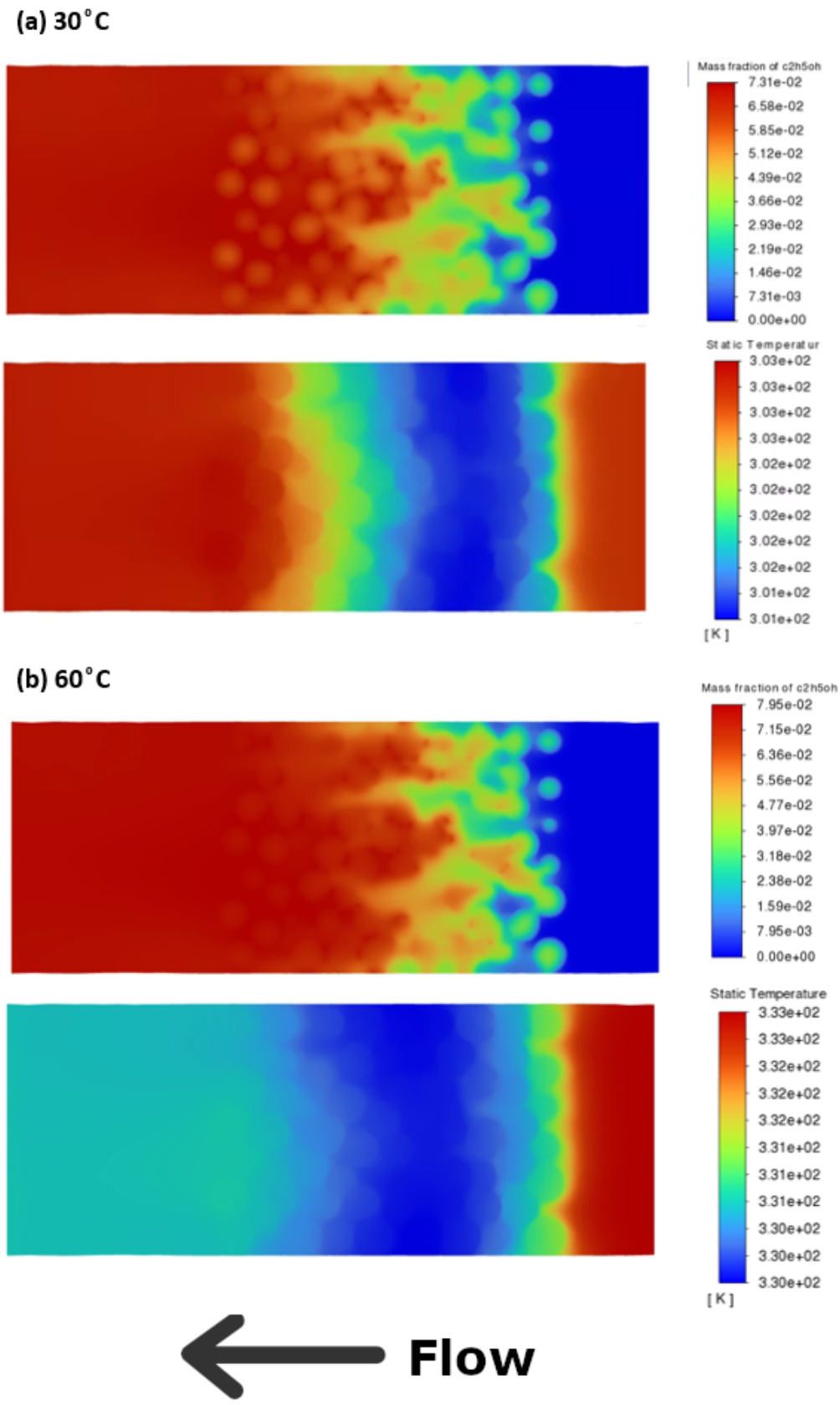

Figure 4.11: Mass fraction of ethanol and temperature contours along the bed at the mid-plane (x=0) at time = 60s after desorption starts.

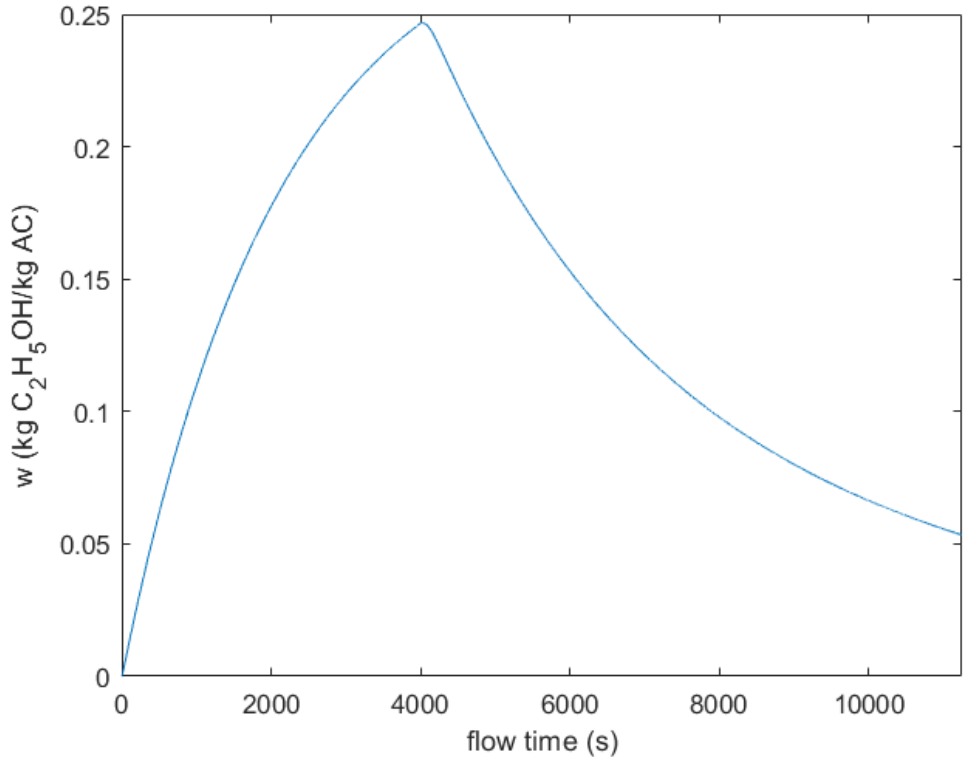

Figure 4.12: Volume-averaged adsorbed amount (w) profile during adsorption-desorption cycle at 30°C.

Figure 4.12 shows the volume-averaged adsorbed amount of ethanol in particles as a function of time. After the ethanol shut off, the adsorbed vapor starts to desorb and w decreases as time passes. Figure 4.13 shows the volume-average temperature of the particles during the adsorption desorption cycle. Temperature increases at the beginning of the adsorption which immediately starts when the ethanol vapor diffused in the system and then decreases as the adsorption rate decreases. After the ethanol shut off, particles the temperature of the particles started to decrease because of the nature of desorption, and then increases with the decreasing rate of desorption.

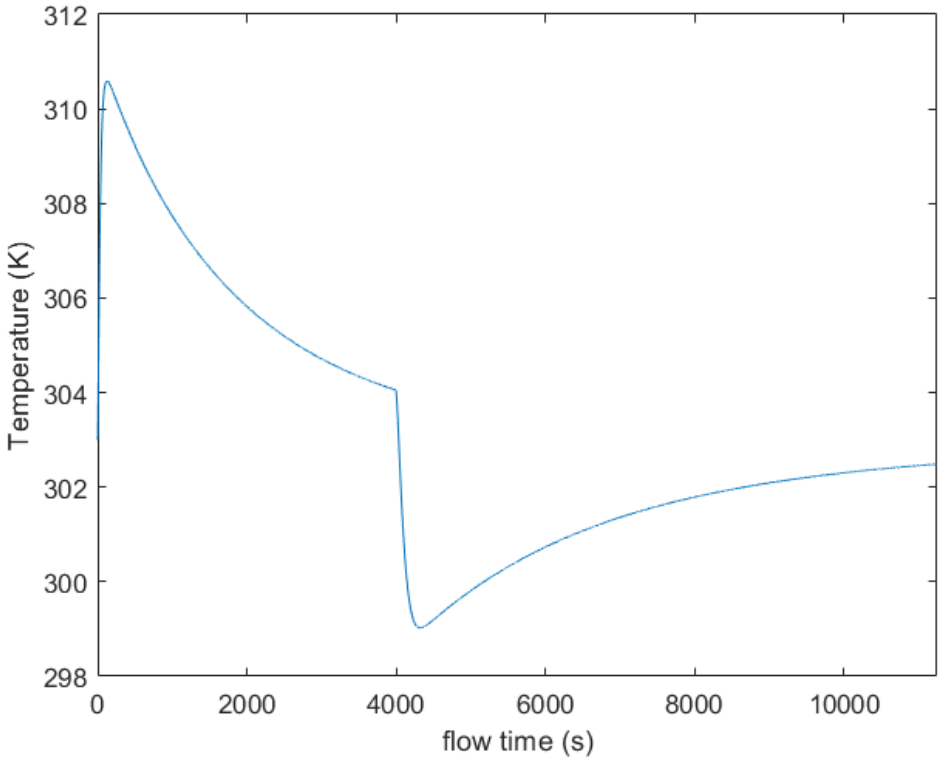

Figure 4.13: Volume-averaged temperature profile of particles during adsorption-desorption cycle at 30°C.

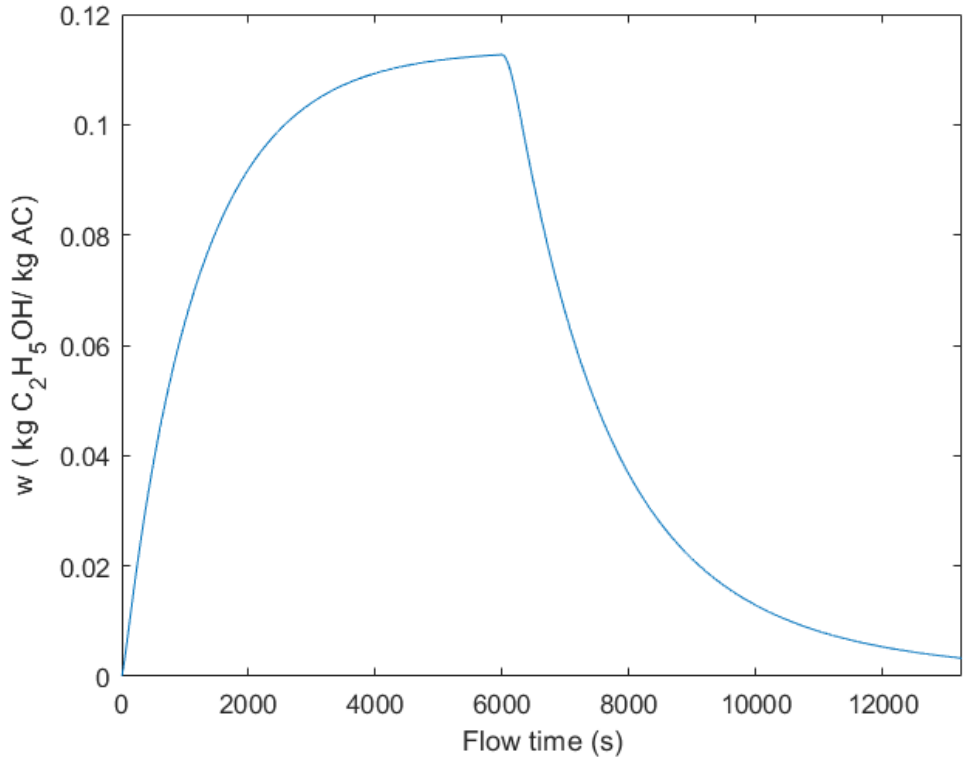

Figure 4.14: Volume-averaged adsorbed amount (w) profile during adsorption-desorption cycle at 60°C.

Similarly, the adsorption-desorption cycle performed at 60°C have lower adsorption rate but higher desorption rate due to increased temperature as Figure 4.14 demonstrates. Even though the time passed after desorption starts is the same in Figure 4.12 and Figure 4.14, adsorbed vapor amount almost vanishes at the end of the time at 60°C; however, it still needs so much time to for complete desorption in 30°C. The temperature profile shows a similar manner as described in Figure 4.15. Particles reached the inflow temperature at 60°C in a shorter time than observed in 30°C. It still requires that time to reach the complete desorption to have the inflow temperature.

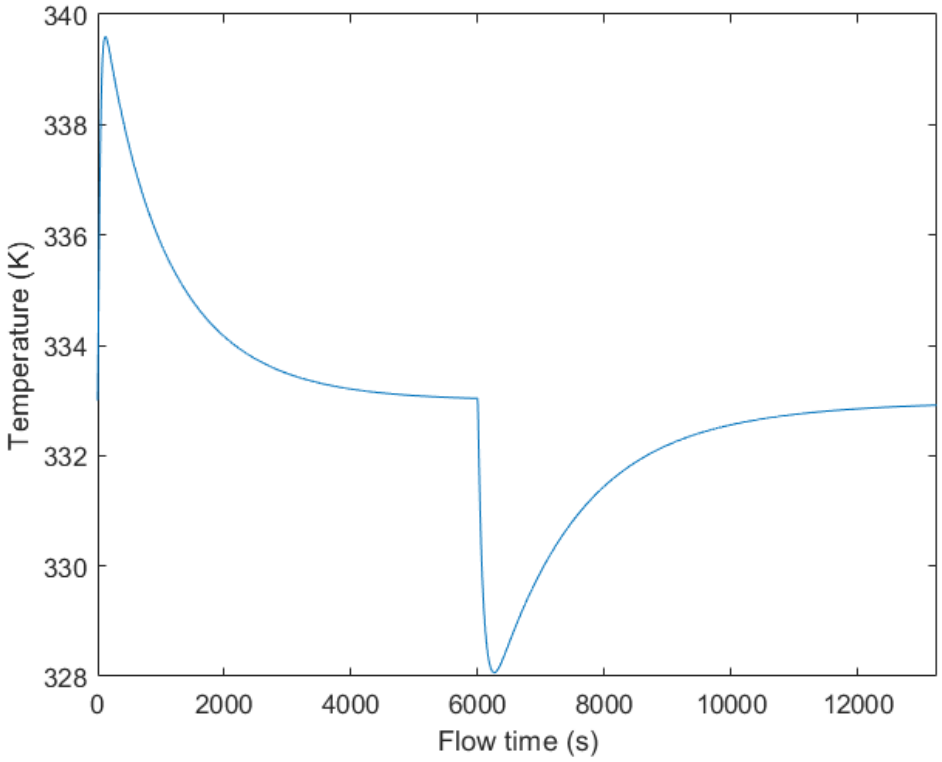

Figure 4.15: Volume-average temperature of particles during adsorption-desorption cycle at 60°C.

CHAPTER 5

CONCLUSIONS AND FUTURE WORK

5.1 Conclusions

In this study, the packed adsorption bed of an adsorption-based ethanol/activated carbon chemical heat pump was investigated both theoretically and computationally. Using Discrete Element Method, a randomly packed structure of the bed having a tube-to-particle diameter ratio of 7 was generated. Then, using Computational Fluid Dynamics, the reactor bed was 3D simulated to observe the hydrodynamic characteristics and adsorption-desorption characteristics at 30 °C and 60 °C operations.

The results showed that the model captures flow, heat and mass transfer phenomena in the adsorption-desorption process in a packed medium by allowing the unsteady inspection of them. Findings demonstrated that not only the flow field and regime can be examined, but also the reaction regime being diffusion-controlled or kinetically-controlled can be investigated. The approach provided an observation of complex transport phenomena and their local effects arising from the random nature of the bed. The overall temperature and adsorbed concentration results of the bed were found to be consistent with the relevant works; thus, the transient response of these local effects on the overall system can be inquired for the design step without approximating the bed to a continuous medium.

5.2 Future Work

Parametric simulations can further improve the study in terms of physical and geometric. Varying structural parameters with different materials and different tube-

to-particle diameter ratios should be used and compared to see the relative rates of transport mechanisms locally with their effects on the overall.

Different operating conditions such as temperature, velocity and heat transfer conditions should be employed to achieve the optimum design of the bed. The developed model can be used as a methodology for packed-bed adsorption systems with small tube-to-particle diameter ratios to further investigate the critical parameters with hydrodynamic and thermal effects. The studies can be utilized to deduce an effective property for the overall bed and may be a useful tool to fill the gap between the conventional and particle-resolved models.

REFERENCES

[1] N. Jurtz, M. Kraume, and G. D. Wehinger, "Advances in fixed-bed reactor modeling using particle-resolved computational fluid dynamics (cfd)," *Reviews in Chemical Engineering*, vol. 35, no. 2, pp. 139–190, 2019.

[2] G. D. Wehinger, *Particle-resolved CFD simulations of catalytic flow reactors*. PhD thesis, Technische Universitaet Berlin (Germany), 2016.

[3] S. Bu, J. Yang, M. Zhou, S. Li, Q. Wang, and Z. Guo, "On contact point modifications for forced convective heat transfer analysis in a structured packed bed of spheres," *Nuclear Engineering and Design*, vol. 270, pp. 21–33, 2014.

[4] A. E. Inc, "Edem user guide, 2022.1 release," 2022. `https://2022.help.altair.com/2022.1/EDEM/index.htm#t=Appendix.htm`.

[5] A. G. Dixon, M. E. Taskin, M. Nijemeisland, and E. H. Stitt, "Cfd method to couple three-dimensional transport and reaction inside catalyst particles to the fixed bed flow field," *Industrial & Engineering Chemistry Research*, vol. 49, no. 19, pp. 9012–9025, 2010.

[6] W. Wongsuwan, S. Kumar, P. Neveu, and F. Meunier, "A review of chemical heat pump technology and applications," *Applied Thermal Engineering*, vol. 21, no. 15, pp. 1489–1519, 2001.

[7] C. Chan, J. Ling-Chin, and A. Roskilly, "A review of chemical heat pumps, thermodynamic cycles and thermal energy storage technologies for low grade heat utilisation," *Applied Thermal Engineering*, vol. 50, no. 1, pp. 1257–1273, 2013.

[8] H. Demir, M. Mobedi, and S. Ülkü, "A review on adsorption heat pump: Problems and solutions," *Renewable and Sustainable Energy Reviews*, vol. 12, no. 9, pp. 2381–2403, 2008.

[9] E. Anyanwu, "Review of solid adsorption solar refrigerator i: an overview of the refrigeration cycle," *Energy Conversion and Management*, vol. 44, no. 2, pp. 301–312, 2003.

[10] H. Yi, K. Nakabayashi, S.-H. Yoon, and J. Miyawaki, "Study on the applicability of pressurized physically activated carbon as an adsorbent in adsorption heat pumps," *RSC Advances*, vol. 12, pp. 2558–2563, 01 2022.

[11] A. Elsayed, R. K. AL-Dadah, S. Mahmoud, and W. Kaialy, "Investigation of activated carbon/ethanol for low temperature adsorption cooling," *International Journal of Green Energy*, vol. 15, no. 5, pp. 277–285, 2018.

[12] D. Attan, M. Alghoul, B. Saha, J. Assadeq, and K. Sopian, "The role of activated carbon fiber in adsorption cooling cycles," *Renewable and Sustainable Energy Reviews*, vol. 15, no. 3, pp. 1708–1721, 2011.

[13] J. Joshi and K. Nandakumar, "Computational modeling of multiphase reactors," *Annual Review of Chemical and Biomolecular Engineering*, vol. 6, no. 1, pp. 347–378, 2015. PMID: 26134737.

[14] A. G. Dixon, M. Nijemeisland, and E. H. Stitt, "Packed tubular reactor modeling and catalyst design using computational fluid dynamics," in *Computational Fluid Dynamics* (G. B. Marin, ed.), vol. 31 of *Advances in Chemical Engineering*, pp. 307–389, Academic Press, 2006.

[15] S. Ergun, "Fluid flow through packed columns," vol. 48, no. 2, pp. 89–94, 1952.

[16] G. I. Taylor, "Dispersion of soluble matter in solvent flowing slowly through a tube," *Proceedings of the Royal Society of London. Series A. Mathematical and Physical Sciences*, vol. 219, no. 1137, pp. 186–203, 1953.

[17] R. Aris, "On the dispersion of a solute in a fluid flowing through a tube," *Proceedings of the Royal Society of London. Series A. Mathematical and Physical Sciences*, vol. 235, pp. 67 – 77, 1956.

[18] O. Levenspiel and K. Bischoff, "Advances in chemical engineering," *vol*, vol. 4, p. 95, 1963.

[19] J. J. Carberry and M. M. Wendel, "A computer model of the fixed bed catalytic reactor: The adiabatic and quasi-adiabatic cases," *AIChE Journal*, vol. 9, no. 1, pp. 129–133, 1963.

[20] J. M. Smith, "Heat and mass transfer in packed beds, n. wakao and s. kaguei, gordon and breach science publishers, 1983,364 pages," *Aiche Journal*, vol. 29, pp. 1055–1055, 1983.

[21] G. F. FROMENT, *Analysis and Design of Fixed Bed Catalytic Reactors*, ch. 1, pp. 1–55.

[22] D. Kunii and J. Smith, "Heat transfer characteristics of porous rocks," *AIChE Journal*, vol. 6, no. 1, pp. 71–78, 1960.

[23] S. Yagi and D. Kunii, "Studies on heat transfer near wall surface in packed beds," *AIChE Journal*, vol. 6, no. 1, pp. 97–104, 1960.

[24] G. Froment, "Fixed bed catalytic reactors—current design status," *Industrial & Engineering Chemistry*, vol. 59, no. 2, pp. 18–27, 1967.

[25] M.-L. McGuire and L. Lapidus, "On the stability of a detailed packed-bed reactor," *AIChE Journal*, vol. 11, no. 1, pp. 85–95, 1965.

[26] M. Winterberg, E. Tsotsas, A. Krischke, and D. Vortmeyer, "A simple and coherent set of coefficients for modelling of heat and mass transport with and without chemical reaction in tubes filled with spheres," *Chemical Engineering Science*, vol. 55, no. 5, pp. 967–979, 2000.

[27] G. Froment, K. Bischoff, and J. De Wilde, *Chemical Reactor Analysis and Design, 3rd Edition*. John Wiley & Sons, Incorporated, 2010.

[28] M. Giese, K. Rottschäfer, and D. Vortmeyer, "Measured and modeled superficial flow profiles in packed beds with liquid flow," *Aiche Journal*, vol. 44, pp. 484–490, 1998.

[29] C. McGreavy and D. L. Cresswell, "A lumped parameter approximation to a general model for catalytic reactors," *The Canadian Journal of Chemical Engineering*, vol. 47, no. 6, pp. 583–589, 1969.

[30] E. W. Thiele, "Relation between catalytic activity and size of particle," *Industrial & Engineering Chemistry*, vol. 31, no. 7, pp. 916–920, 1939.

[31] R. Bird, W. Stewart, and E. Lightfoot, "Transport phenomena. john wiley & sons, inc," *New York, NY*, vol. 1, 2002.

[32] H. Fogler, "Elements of chemical reaction engineering . boston, ma: Person education," 2006.

[33] B. V. R. Kuncharam and A. G. Dixon, "Multi-scale two-dimensional packed bed reactor model for industrial steam methane reforming," *Fuel Processing Technology*, vol. 200, p. 106314, 2020.

[34] J. Xu and G. F. Froment, "Methane steam reforming, methanation and water-gas shift: I. intrinsic kinetics," *AIChE Journal*, vol. 35, no. 1, pp. 88–96, 1989.

[35] J. Xu and G. F. Froment, "Methane steam reforming: Ii. diffusional limitations and reactor simulation," *AIChE Journal*, vol. 35, no. 1, pp. 97–103, 1989.

[36] C. McGreavy and D. Cresswell, "A lumped parameter approximation to a general model for catalytic reactors," *The Canadian Journal of Chemical Engineering*, vol. 47, no. 6, pp. 583–589, 1969.

[37] N. Wakao and J. Smith, "Diffusion in catalyst pellets," *Chemical Engineering Science*, vol. 17, no. 11, pp. 825–834, 1962.

[38] L. L. Hegedus, "Catalyst pore structures by constrained nonlinear optimization," *Industrial & Engineering Chemistry Product Research and Development*, vol. 19, no. 4, pp. 533–537, 1980.

[39] M. F. Johnson and W. E. Stewart, "Pore structure and gaseous diffusion in solid catalysts," *Journal of Catalysis*, vol. 4, no. 2, pp. 248–252, 1965.

[40] J. Szekely and J. Evans, "A structural model for gas-solid reactions with a moving boundary-ii: The effect of grain size, porosity and temperature on the reaction of porous pellets," *Chemical Engineering Science*, vol. 26, no. 11, pp. 1901–1913, 1971.

[41] Z. Wang, A. Afacan, K. Nandakumar, and K. Chuang, "Porosity distribution in random packed columns by gamma ray tomography," *Chemical Engineering and Processing: Process Intensification*, vol. 40, no. 3, pp. 209–219, 2001. Funding Information: The authors are grateful to the Environmental Sciences and Technology Alliance Canada (ESTAC) and the Natural Science and Engineering Research Council of Canada (NSERC) for the financial support for this research.

[42] X. Yang, T. D. Scheibe, M. C. Richmond, W. A. Perkins, S. J. Vogt, S. L. Codd, J. D. Seymour, and M. I. McKinley, "Direct numerical simulation of pore-scale flow in a bead pack: Comparison with magnetic resonance imaging observations," *Advances in water resources*, vol. 54, pp. 228–241, 2013.

[43] R. Caulkin, W. Tian, M. Pasha, A. Hassanpour, and X. Jia, "Impact of shape representation schemes used in discrete element modelling of particle packing," *Computers & Chemical Engineering*, vol. 76, pp. 160–169, 2015.

[44] R. Caulkin, X. Jia, C. Xu, M. Fairweather, R. A. Williams, H. Stitt, M. Nijemeisland, S. Aferka, M. Crine, A. Léonard, D. Toye, and P. Marchot, "Simulations of structures in packed columns and validation by x-ray tomography," *Industrial & Engineering Chemistry Research*, vol. 48, no. 1, pp. 202–213, 2009.

[45] Y. Duan, M. Xu, X. Zhou, and X. Huai, "A structured packed-bed reactor designed for exothermic hydrogenation of acetone," *Particuology*, vol. 17, pp. 125–130, 2014.

[46] X. Zhou, Y. Duan, X. Huai, and X. Li, "3d cfd modeling of acetone hydrogenation in fixed bed reactor with spherical particles," *Particuology*, vol. 11, no. 6, pp. 715–722, 2013.

[47] A. Dixon, M. Nijemeisland, and E. Stitt, "Systematic mesh development for 3d cfd simulation of fixed beds: Contact points study," *Computers Chemical Engineering*, vol. 48, p. 135–153, 01 2013.

[48] J. Yang, Q. Wang, M. Zeng, and A. Nakayama, "Computational study of forced convective heat transfer in structured packed beds with spherical or ellipsoidal particles," *Chemical Engineering Science*, vol. 65, no. 2, pp. 726–738, 2010.

[49] J. Yang, J. Wang, S. Bu, M. Zeng, Q. Wang, and A. Nakayama, "Experimental analysis of forced convective heat transfer in novel structured packed beds of particles," *Chemical Engineering Science*, vol. 71, pp. 126–137, 2012.

[50] A. G. Dixon, A. K. Gurnon, M. Nijemeisland, and E. H. Stitt, "Cfd testing of the pointwise use of the zehner–schlünder formulas for fixed-bed stagnant thermal conductivity," *International Communications in Heat and Mass Transfer*, vol. 42, pp. 1–4, 2013.

[51] A. G. Dixon, M. Ertan Taskin, E. Hugh Stitt, and M. Nijemeisland, "3d cfd simulations of steam reforming with resolved intraparticle reaction and gradients," *Chemical Engineering Science*, vol. 62, no. 18, pp. 4963–4966, 2007. 19th International Symposium on Chemical Reaction Engineering - From Science to Innovative Engineering.

[52] S.-H. Cheng, H. Chang, Y.-H. Chen, H.-J. Chen, Y.-K. Chao, and Y.-H. Liao, "Computational fluid dynamics-based multiobjective optimization for catalyst design," *Industrial & Engineering Chemistry Research*, vol. 49, no. 21, pp. 11079–11086, 2010.

[53] T. Atmakidis and E. Kenig, "Cfd-based analysis of the wall effect on the pressure drop in packed beds with moderate tube/particle diameter ratios in the laminar flow regime," *Chemical Engineering Journal - CHEM ENG J*, vol. 155, pp. 404–410, 12 2009.

[54] T. Atmakidis and E. Y. Kenig, "Numerical analysis of residence time distribution in packed bed reactors with irregular particle arrangements," *Chemical Product and Process Modeling*, vol. 10, no. 1, pp. 17–26, 2015.

[55] H. Freund, T. Zeiser, F. Huber, E. Klemm, G. Brenner, F. Durst, and G. Emig, "Numerical simulations of single phase reacting flows in randomly packed fixed-bed reactors and experimental validation," *Chemical Engineering Science*, vol. 58, no. 3, pp. 903–910, 2003. 17th International Symposium of Chemical Reaction Engineering (IS CRE 17).

[56] H. Freund, J. Bauer, T. Zeiser, and G. Emig, "Detailed simulation of transport

processes in fixed-beds," *Industrial & Engineering Chemistry Research*, vol. 44, no. 16, pp. 6423–6434, 2005.

[57] A. Dixon, "Comsol multiphysics ä simulation of 3d single-3 hase transport in a random packed bed of spheres," 2014.

[58] R. Caulkin, A. Ahmad, M. Fairweather, X. Jia, and R. Williams, "Digital predictions of complex cylinder packed columns," *Computers & Chemical Engineering*, vol. 33, pp. 10–21, 01 2009.

[59] P. A. Cundall and O. D. L. Strack, "A discrete numerical model for granular assemblies," *Géotechnique*, vol. 29, no. 1, pp. 47–65, 1979.

[60] A. Di Renzo and F. P. Di Maio, "Comparison of contact-force models for the simulation of collisions in dem-based granular flow codes," *Chemical Engineering Science*, vol. 59, no. 3, pp. 525–541, 2004.

[61] Y. Dong, M. Geske, O. Korup, N. Ellenfeld, F. Rosowski, C. Dobner, and R. Horn, "What happens in a catalytic fixed-bed reactor for n-butane oxidation to maleic anhydride? insights from spatial profile measurements and particle resolved cfd simulations," *Chemical Engineering Journal*, vol. 350, pp. 799–811, 2018.

[62] G. D. Wehinger, T. Eppinger, and M. Kraume, "Detailed numerical simulations of catalytic fixed-bed reactors: Heterogeneous dry reforming of methane," *Chemical Engineering Science*, vol. 122, pp. 197–209, 2015.

[63] T. Eppinger, K. Seidler, and M. Kraume, "Dem-cfd simulations of fixed bed reactors with small tube to particle diameter ratios," *Chemical Engineering Journal*, vol. 166, no. 1, pp. 324–331, 2011.

[64] J.-j. Lee, S.-J. Yoon, Ph.D., G.-C. PARK, and W. Lee, "Turbulence-induced heat transfer in pbmr core using les and rans," *Journal of Nuclear Science and Technology*, vol. 44, pp. 985–996, 07 2007.

[65] S. A. Ookawara, M. Kuroki, D. Street, and K. Ogawaa, "High-fidelity dem-cfd modeling of packed bed reactors for process intensification," 2007.

[66] E. A. Daymo, M. Hettel, O. Deutschmann, and G. D. Wehinger, "Accelerating particle-resolved cfd simulations of catalytic fixed-bed reactors with duo," *Chemical Engineering Science*, vol. 250, p. 117408, 2022.

[67] U. Maas and S. B. Pope, "Simplifying chemical kinetics: intrinsic low-dimensional manifolds in composition space," *Combustion and flame*, vol. 88, no. 3-4, pp. 239–264, 1992.

[68] G. M. Goldin, Z. Ren, and S. Zahirovic, "A cell agglomeration algorithm for accelerating detailed chemistry in cfd," *Combustion Theory and Modelling*, vol. 13, no. 4, pp. 721–739, 2009.

[69] M. Bracconi, M. Maestri, and A. Cuoci, "In situ adaptive tabulation for the cfd simulation of heterogeneous reactors based on operator-splitting algorithm," *AIChE Journal*, vol. 63, no. 1, pp. 95–104, 2017.

[70] C. Strassacker, V. Bykov, and U. Maas, "Redim reduced modeling of quenching at a cold wall including heterogeneous wall reactions," *International Journal of Heat and Fluid Flow*, vol. 69, pp. 185–193, 2018.

[71] L. Liang, J. G. Stevens, and J. T. Farrell, "A dynamic adaptive chemistry scheme for reactive flow computations," *Proceedings of the Combustion Institute*, vol. 32, no. 1, pp. 527–534, 2009.

[72] D. Kandhai, D. Vidal, A. Hoekstra, H. Hoefsloot, P. Iedema, and P. Sloot, "A comparison between lattice-boltzmann and finite-element simulations of fluid flow in static mixer reactors," *International Journal of Modern Physics C*, vol. 9, pp. 1123–1128, 12 1998.

[73] T. Zeiser, P. Lammers, E. Klemm, Y.-W. Li, J. Bernsdorf, and G. Brenner, "Cfd-calculation of flow, dispersion and reaction in a catalyst filled tube by the lattice boltzmann method," *Chemical Engineering Science*, vol. 56, pp. 1697–1704, 02 2001.

[74] B. Manz, L. F. Gladden, and P. B. Warren, "Flow and dispersion in porous media: Lattice-boltzmann and nmr studies," *AIChE Journal*, vol. 45, no. 9, pp. 1845–1854, 1999.

[75] W. Kwapinski, K. Salem, D. Mewes, and E. Tsotsas, "Thermal and flow effects during adsorption in conventional, diluted and annular packed beds," *Chemical Engineering Science*, vol. 65, no. 14, pp. 4250–4260, 2010.

[76] P. Hu, S. Wang, J. Wang, S. Jiang, Y. Liang, Z. Ma, and S. Gao, "Thermal performance analysis of the sorption heat storage system with packed bed based on a spatially resolved 2d model," *Sustainable Energy Technologies and Assessments*, vol. 49, p. 101753, 2022.

[77] F. Augier, C. Laroche, and E. Brehon, "Application of computational fluid dynamics to fixed bed adsorption calculations: Effect of hydrodynamics at laboratory and industrial scale," *Separation and Purification Technology*, vol. 63, no. 2, pp. 466–474, 2008.

[78] Z. Yan, S. Wilkinson, E. Stitt, and M. Marigo, "Discrete element modelling (dem) input parameters: understanding their impact on model predictions using statistical analysis," *Computational Particle Mechanics*, vol. 2, pp. 283–299, 2015.

[79] M. Marigo and E. H. Stitt, "Discrete element method (dem) for industrial applications: comments on calibration and validation for the modelling of cylindrical pellets," *KONA Powder and Particle Journal*, vol. 32, pp. 236–252, 2015.

[80] Y. Li, Y. Xu, and C. Thornton, "A comparison of discrete element simulations and experiments for 'sandpiles' composed of spherical particles," *Powder Technology*, vol. 160, no. 3, p. 219 – 228, 2005. Cited by: 275.

[81] L. Adr, N. Rg, and P. Gauché, "A dem-cfd approach to predict the pressure drop through an air-rock bed thermal energy storage system: Part 2 of 2," 2012.

[82] B. E. Launder and D. B. Spalding, "Lectures in mathematical models of turbulence," *(No Title)*, 1972.

[83] A. Dybbs and R. V. Edwards, *A New Look at Porous Media Fluid Mechanics — Darcy to Turbulent*, pp. 199–256. Dordrecht: Springer Netherlands, 1984.

[84] E. N. Fuller, P. D. Schettler, and J. C. Giddings, "New method for prediction of binary gas-phase diffusion coefficients," *Industrial & Engineering Chemistry*, vol. 58, no. 5, pp. 18–27, 1966.

[85] A. O. Yurtsever, G. Karakas, and Y. Uludag, "Modeling and computational simulation of adsorption based chemical heat pumps," *Applied Thermal Engineering*, vol. 50, no. 1, pp. 401–407, 2013.

[86] E. P. Linstrom and W. Mallard, *NIST Chemistry WebBook, NIST Standard Reference Database Number 69*. National Institute of Standards and Technology, Gaithersburg MD, 20899, 2023 (retrieved September 1, 2023).

[87] J. Y. Murthy and S. R. Mathur, "Computation of Anisotropic Conduction Using Unstructured Meshes," *Journal of Heat Transfer*, vol. 120, pp. 583–591, 08 1998.

APPENDIX A

VELOCITY HISTOGRAMS

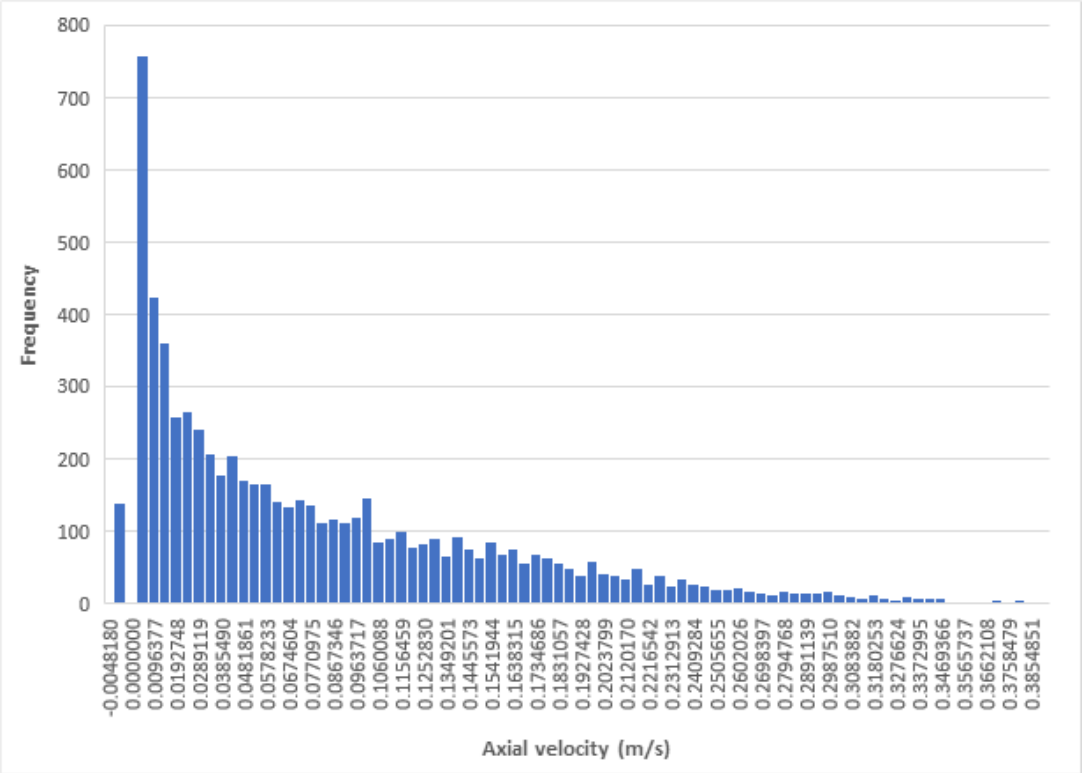

Figure A.1: Histogram of axial velocities on the radial plane at z = 0.

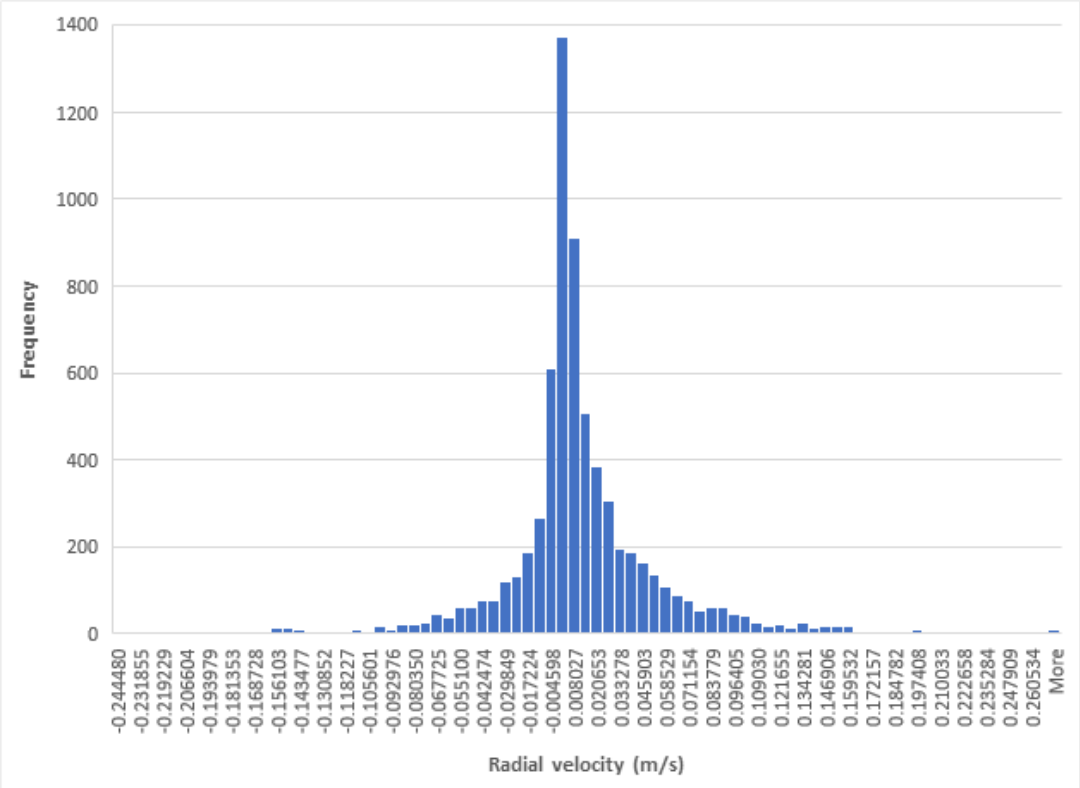

Figure A.2: Histogram of radial velocities on the radial plane at z = 0.

APPENDIX B

MESH INDEPENDENCY STUDY

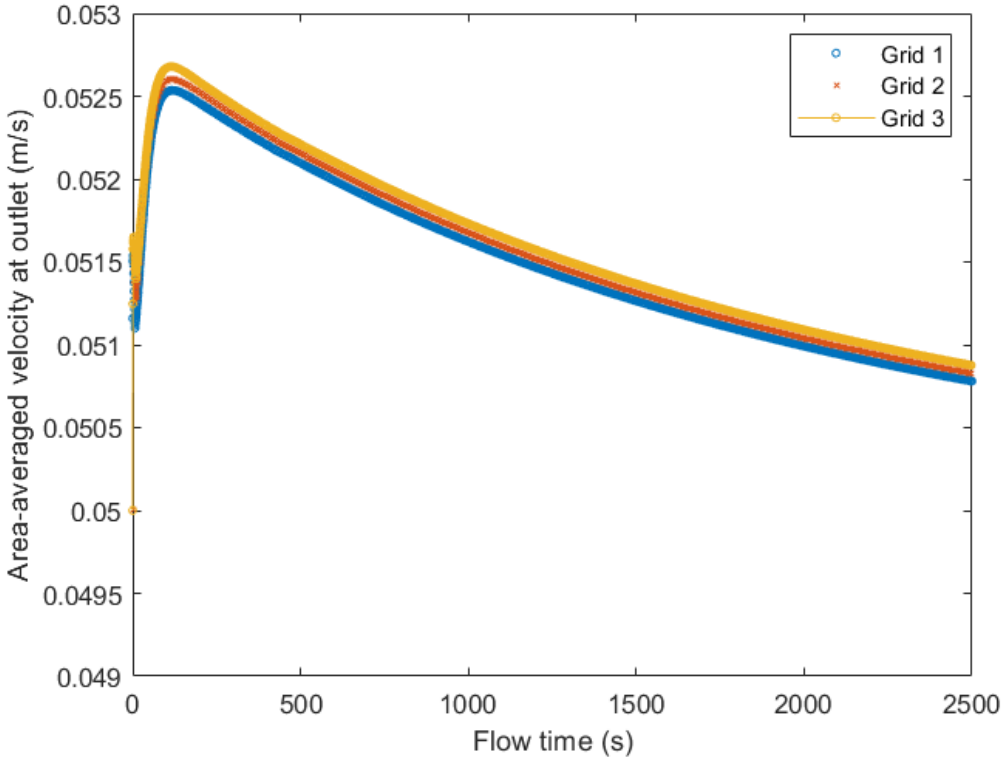

Figure B.1: Outlet velocity profiles of different grids.

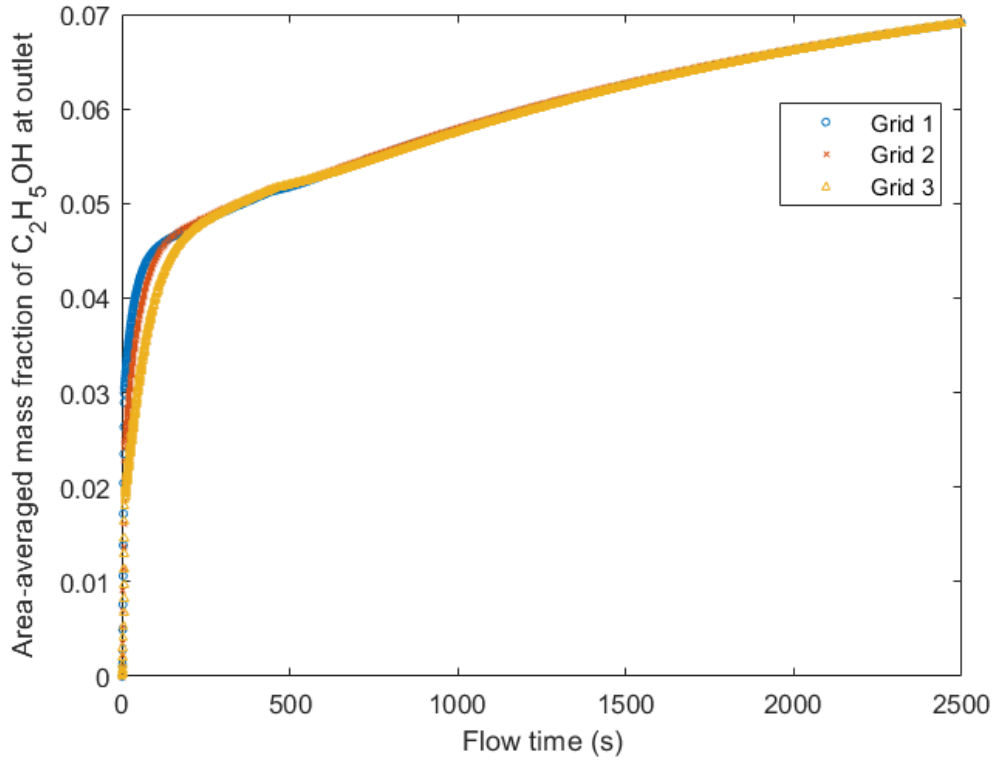

Figure B.2: Outlet mass fraction of C_2H_5OH profiles of different grids.

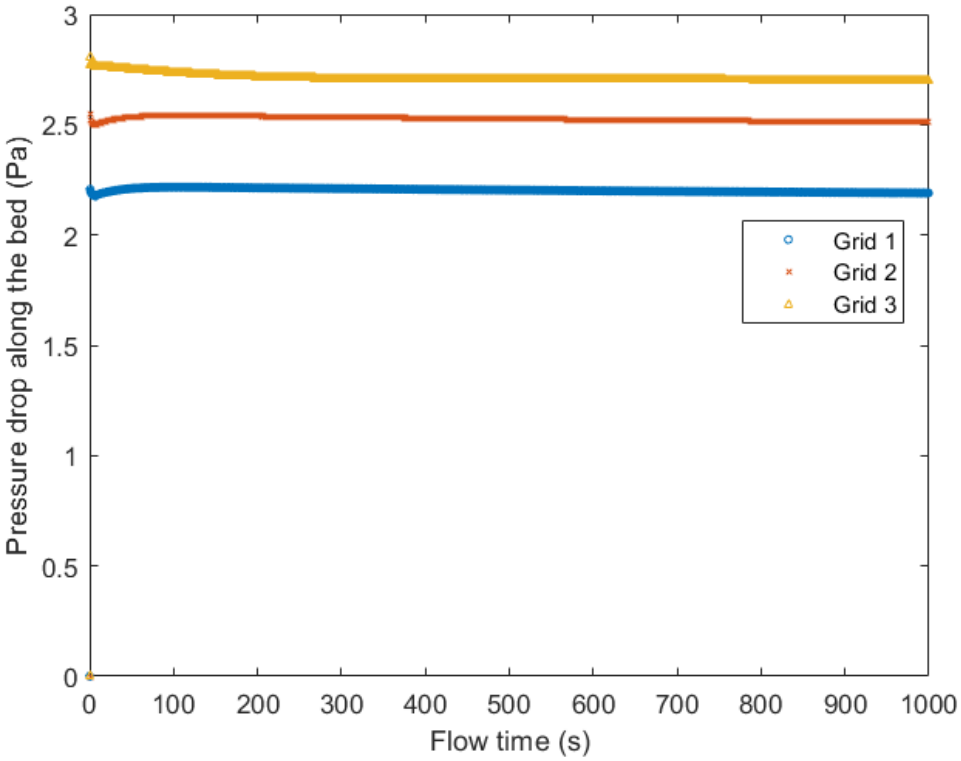

Figure B.3: Pressure drop along the bed for different grids.

APPENDIX C

CODE SCRIPTS USED IN THE MODEL

C.1 Geometry Generation Routine

```
#Author- silayonder
#Description- This code generates randomly packed bed of spheres
↪  with local bridges

import adsk.core, adsk.fusion, adsk.cam, traceback, math

def run(context):
    ui = None
    try:
        app = adsk.core.Application.get()
        ui  = app.userInterface

        des = app.activeProduct
        root = des.rootComponent
        bodies = root.bRepBodies

        des.designType = adsk.fusion.DesignTypes.DirectDesignType

        radius = 0.001    # Sphere radius in m
        r2 = radius*0.25    # Cylinder radius in m

        threShold = radius*0.07
        TankC1 = adsk.core.Point3D.create(0,0,-0.011)
        TankC2 = adsk.core.Point3D.create(0,0,0.011)
        TankRadius = 0.00701
```

```
# Read sphere center positions from files
x =
↪  open('C:/Users/onder/Desktop/UDF1/MyFirstScript/small__X.txt',
↪  'r')
linesx = x.readlines()

y =
↪  open('C:/Users/onder/Desktop/UDF1/MyFirstScript/small__Y.txt',
↪  'r')
linesy = y.readlines()

z =
↪  open('C:/Users/onder/Desktop/UDF1/MyFirstScript/small__Z.txt',
↪  'r')
linesz = z.readlines()


tBrep = adsk.fusion.TemporaryBRepManager.get()
sphereBody = None
centerArray = []
lineArray = []
sphereArray = []
cylinderArray = []
wallCylinderArray = []

# Generate center points
for i in range(len(linesx)):
    center = adsk.core.Point3D.create(float(linesx[i]),
    ↪  float(linesy[i]), float(linesz[i]))
    line = adsk.core.Point3D.create(0, 0, float(linesz[i]))
    centerArray.append(center)
    lineArray.append(line)

    # Generate spheres
    sphereBody = tBrep.createSphere(center, radius)
    sphereArray.append(sphereBody)
```

```
# Generate cylinder between spheres
for i in range(len(centerArray)):
    for j in range(len(centerArray)):
        if i == j:
            continue
        p1 = centerArray[i]
        p2 = centerArray[j]
        distance = p1.distanceTo(p2)
        DirVec = p1.vectorTo(p2)
        DirVec.normalize()
        DirVec_rad = adsk.core.Vector3D.create(DirVec.x *
        ↪  radius * 0.6, DirVec.y * radius * 0.6, DirVec.z
        ↪  * radius * 0.6)

        DirVec_rad_pt =
        ↪  adsk.core.Point3D.create(DirVec_rad.x,
        ↪  DirVec_rad.y, DirVec_rad.z)
        p1_translated = adsk.core.Point3D.create((p1.x -
        ↪  DirVec_rad_pt.x), (p1.y - DirVec_rad_pt.y),
        ↪  (p1.z - DirVec_rad_pt.z))
        p2_translated = adsk.core.Point3D.create((p2.x +
        ↪  DirVec_rad_pt.x), (p2.y + DirVec_rad_pt.y),
        ↪  (p2.z + DirVec_rad_pt.z))

        if (distance - 2 * radius) <= threShold:
            cylinder =
            ↪  tBrep.createCylinderOrCone(p1_translated,
            ↪  r2, p2_translated, r2)
            cylinderArray.append(cylinder)

# Generate cylinder bed
TankCylinder = tBrep.createCylinderOrCone(TankC1,
↪  TankRadius, TankC2, TankRadius)
body3 = bodies.add(TankCylinder)
body3.name = 'Tank Cylinder'
```

```
# Generate cylinder between bed wall and spheres
for i in range(len(centerArray)):
    c1 = centerArray[i]
    dist1 = abs(math.sqrt((c1.x) ** 2 + (c1.y) ** 2))
    dist2 = TankRadius - dist1 - radius
    DirVec2 = c1.asVector()
    DirVec2.z = 0
    DirVec2 = adsk.core.Vector3D.create(c1.x, c1.y, 0)
    DirVec2.normalize()
    DirVec_rad2 = adsk.core.Vector3D.create((DirVec2.x *
    ↪  radius *0.6), (DirVec2.y) * radius * 0.6,
    ↪  (DirVec2.z) * radius * 0.6)
    DirVec_rad3 = adsk.core.Vector3D.create((DirVec2.x *
    ↪  radius * 1.5), (DirVec2.y) * radius * 1.5,
    ↪  (DirVec2.z) * radius * 1.5)
    DirVec_rad_pt2 =
    ↪  adsk.core.Point3D.create(DirVec_rad2.x,
    ↪  DirVec_rad2.y, DirVec_rad2.z)
    DirVec_rad_pt3 =
    ↪  adsk.core.Point3D.create(DirVec_rad3.x,
    ↪  DirVec_rad3.y, DirVec_rad3.z)
    c2_translated = adsk.core.Point3D.create((c1.x +
    ↪  DirVec_rad_pt3.x), (c1.y + DirVec_rad_pt3.y), (c1.z
    ↪  + DirVec_rad_pt2.z))

    if dist2 <= threShold:
        wallcylinder = tBrep.createCylinderOrCone(c1, r2,
        ↪  c2_translated, r2)
        wallCylinderArray.append(wallcylinder)


# Union all of the created objects
sp = sphereArray[0]
union = adsk.fusion.BooleanTypes.UnionBooleanType
for i in range(1, len(sphereArray)):
    tBrep.booleanOperation(sp, sphereArray[i], union)
```

```
        for i in range(len(cylinderArray)):
            tBrep.booleanOperation(sp, cylinderArray[i], union)

        for i in range(len(wallCylinderArray)):
            tBrep.booleanOperation(sp, wallCylinderArray[i], union)

        body = bodies.add(sp)
        body.name = 'Booleaned Bodies'

    except:
        if ui:
            ↪ ui.messageBox('Failed:\n{}'.format(traceback.format_exc()))
```

C.2 ANSYS Fluent User-Defined Functions

C.2.1 Interface Boundary Condition

```
#include "udf.h"
#include "sg.h"
#include "mem.h"
#include "math.h"

DEFINE_PROFILE(int_bc_Ys, t, nv)
{
    face_t f;
    real ds0, ds1;
    real A_by_es0, A_by_es1;
    real NV_VEC(es0), NV_VEC(es1);
    real S0, S1, h0, h1, gamma0, gamma1;
    real A[ND_ND];
    Thread* t0, * t1;
    real xf[ND_ND];

    begin_f_loop(f, t)
```

```
    {
        cell_t c0 = F_C0(f, t);      /*  Solid side of the face  */
        cell_t c1 = F_C1(f, t);      /*  Fluid side of the face  */
        t0 = THREAD_T0(t);        /*  Solid side cell thread  */
        t1 = THREAD_T1(t);        /*  Fluid side cell thread    */
        gamma0 = C_DIFF_L(c0, t0, 0, 1);     /*  Solid side thermal
↪  conductivity    */
        gamma1 = C_DIFF_EFF(c1, t1, 0);     /*  Fluid side
↪  diffusion coefficient   */
        real xc0[ND_ND];        /*  Solid cell centroid   */
        real xc1[ND_ND];        /*  Fluid cell centroid    */
        real phi0;
        real phi1;

        F_AREA(A, f, t);       /*  Check if A here is in the
↪  opposite of the flux direction    */
        C_CENTROID(xc0, c0, t0);            /*  Solid cell centroid
↪  coordinates */
        C_CENTROID(xc1, c1, t1);            /*  Fluid cell centroid
↪  coordinates   */
        F_CENTROID(xf, f, t);

        ds0 = sqrt(pow((xf[0] - xc0[0]), 2) + pow((xf[1] - xc0[1]),
↪  2) + pow((xf[2] - xc0[2]), 2));
        ds1 = sqrt(pow((xc1[0] - xf[0]), 2) + pow((xc1[1] - xf[1]),
↪  2) + pow((xc1[2] - xf[2]), 2));
        NV_D(es0, =, (xf[0] - xc0[0]), (xf[1] - xc0[1]), (xf[2] -
↪  xc0[2]));     /*  Unit vector pointing from solid cell center
↪  to face    */
        NV_D(es1, =, (-xc1[0] + xf[0]), (-xc1[1] + xf[1]), (-xc1[2]
↪  + xf[2]));  /*  Unit vector pointing from fluid cell center to
↪  face    */
        A_by_es0 = NV_DOT(A, A) / NV_DOT(A, es0);
        A_by_es1 = NV_DOT(A, A) / NV_DOT(A, es1);
        h0 = gamma0 * A_by_es0 / ds0;
        h1 = -gamma1 * A_by_es1 / ds1;
```

```
        phi0 = C_YI(c0, t0, 0);     /*  Cell value in solid side
↪   */
        phi1 = C_YI(c1, t1, 0);     /*  Cell value in fluid side
↪   */

        F_PROFILE(f, t, nv) =
            ((h0 * phi0 + h1 * phi1) / (h0 + h1));

    }
    end_f_loop(f, t)
}
```

C.2.2 Source terms for adsorption, species transport and energy equations

```
#include "udf.h"
#include "sg.h"
#include "mem.h"
#include "math.h"

#define W0 0.3955
#define D 0.0006049
#define n 1.156
#define A 5.24677   /*  Antoine constant for EtOH   */
#define B 1598.673  /*  Antoine constant for EtOH   */
#define C -46.424   /*  Antoine constant for EtOH   */
#define R 0.00008314 /* Gas constant in m3bar/molK  */
#define MW 0.046    /*  Molar mass of EtOH in kg/mol    */

DEFINE_SOURCE(w_source, c, t, dS, eqn)
{
    real ksav;
    real W;
    real Ps;
    real Pi;
    real w;
    real source;
```

```
    Ps = pow(10.0, (A - (B / (C_T(c, t) + C))));    /*Calculate
↪   vapor pressure by Antoine in bar*/
    Pi = C_R(c, t) * C_YI(c, t, 0) * C_T(c, t) * R / MW;
    W = W0 * exp(-D * pow((C_T(c, t) * log(Ps / (Pi + SMALL))),
↪   n));  /*Adsorption capacity in kg/kg*/
    ksav = 0.58 * exp(-1970.0 / C_T(c, t));
    w = C_UDSI(c, t, 0);    /*Amount adsorbed in kg/kg*/

    source = ksav*(W-w);

    return source;

}
}


#include "udf.h"
#include "sg.h"
#include "mem.h"
#include "math.h"

#define W0 0.3955
#define D 0.0006049
#define n 1.156
#define A 5.24677   /*  Antoine constant for EtOH   */
#define B 1598.673  /*  Antoine constant for EtOH   */
#define C -46.424   /*  Antoine constant for EtOH   */
#define R 0.00008314 /* Gas constant in m3bar/molK  */
#define MW 0.046    /*  Molar mass of EtOH in kg/mol    */
#define RHOS 750.0 /*   Solid density of particle in kg/m3  */
#define EPS 0.35    /*  Particle porosity   */

DEFINE_SOURCE(c_source, c, t, dS, eqn)
{
    real ksav;
    real W;
    real Ps;
```

```
    real Pi;
    real w;
    real source;
    real dwdt;

    Ps = pow(10.0, (A - (B / (C_T(c, t) + C))));    /*Calculate
↪   vapor pressure by Antoine in bar*/
    Pi = C_R(c, t) * R * C_YI(c, t, 0) * C_T(c, t) / MW;
    W = W0 * exp(-D * pow((C_T(c, t) * log(Ps / (Pi + SMALL))),
↪   n));  /*Adsorption capacity in kg/kg*/
    ksav = 0.58 * exp(-1970.0 / C_T(c, t));
    w = C_UDSI(c, t, 0);    /*Amount adsorbed in kg/kg*/

    dwdt = ksav*(W-w);

    source = -(1.0 - EPS) * RHOS * dwdt / (EPS);

    return source;
}


#include "udf.h"
#include "sg.h"
#include "mem.h"
#include "math.h"

#define W0 0.3955
#define D 0.0006049
#define n 1.156
#define A 5.24677   /*  Antoine constant for EtOH   */
#define B 1598.673  /*  Antoine constant for EtOH   */
#define C -46.424   /*  Antoine constant for EtOH   */
#define R 0.00008314 /* Gas constant in m3bar/molK  */
#define MW 0.046    /*  Molar mass of EtOH in kg/mol    */
#define RHOS 750.0 /*   Solid density of particle in kg/m3  */
#define EPS 0.35    /*  Particle porosity   */

DEFINE_SOURCE(en_source, c, t, dS, eqn)
```

```
{
    real ksav;
    real W;
    real Ps;
    real Pi;
    real w;
    real source;
    real dwdt;
    real deltaH;

    Ps = pow(10.0, (A - ( B / (C_T(c, t) + C))));    /* Calculate
↪   vapor pressure by Antoine in bar  */
    Pi = C_R(c, t) * R * C_YI(c, t, 0) * C_T(c, t) / MW;
    W = W0 * exp(-D * pow((C_T(c, t) * log(Ps / (Pi + SMALL))),
↪   n));  /*    Adsorption capacity in kg/kg    */
    ksav = 0.58 * exp(-1970.0 / C_T(c, t));
    w = C_UDSI(c, t, 0);    /*  Amount adsorbed in kg/kg    */

    dwdt = ksav*(W - w);

    deltaH = (30.0 + 0.057 * C_T(c, t))*1000.0;   /*    Heat of
↪   adsorption in J/mol */

    source = (1.0 - EPS) * RHOS * dwdt * deltaH / MW;    /* Heat
↪   source term in W/m3 of porous medium   */

    return source;

}
```

C.2.3 Diffusivity for the domain geometry

```
#include "udf.h"
#include "sg.h"
#include "mem.h"
#include "math.h"
```

```
#define dpore 0.000000004   /*  Pore diameter for particle in m */
#define R 8.314 /*  Gas constant in J/molK    */
#define MW 0.046    /*  Molar mass of EtOH in kg/mol    */
#define MWA 46.0  /*    Molar mass of EtOH in g/mol */
#define MWB 28.0 /* Molar mass of N2 in g/mol    */
#define VA 50.36 /* Diffusion volume of EtOH */
#define VB 17.9 /*  Diffusion volume of N2    */
#define P 1.01325 /*    1 atm   */
#define pi 3.14159


DEFINE_DIFFUSIVITY(diff_coeff, c, thread, i)
{
    real diff;
    real sphereID = 13;   /*Solid ID for particle cell zone*/
    real fluidID = 12;    /*Fluid ID for fluid cell zone*/

    if (THREAD_ID(thread) == sphereID)
    {
        diff = (dpore/3.0) * sqrt((8.0*R*C_T(c, thread))/(pi*MW));
    }

    else
    {
        diff = ((0.001*pow(C_T(c, thread), 1.75) * sqrt(1.0/MWA +
↪   1.0/MWB)) / (P*(pow(VA, 1.0/3.0) + pow(VB, 1.0/3.0))*(pow(VA,
↪   1.0/3.0) + pow(VB, 1.0/3.0)))) * 0.0001;
    }

        return diff;
}
```

C.2.4 Step boundary condition at the inlet

```
#include "udf.h"
#include "unsteady.h"

DEFINE_PROFILE(inletBC, t, nv)
{
    face_t f;


    if (CURRENT_TIME >= 0.0 && CURRENT_TIME < 6000.0)
    {
        begin_f_loop(f, t)
        {
            F_PROFILE(f, t, nv) = 0.08;
        }
        end_f_loop(f, t)
    }

    else if (CURRENT_TIME >= 6000.0)
    {
        begin_f_loop(f, t)
        {
            F_PROFILE(f, t, nv) = 0.0;
        }
    }

}
```